J. Fluid Mech. (2000), *vol.* 419, *pp.* 283–323. Printed in the United Kingdom

© 2000 Cambridge University Press

Compressible magnetoconvection in three dimensions: pattern formation in a strongly stratified layer

By A. M. RUCKLIDGE, N. O. WEISS, D. P. BROWNJOHN, P. C. MATTHEWS† AND M. R. E. PROCTOR

Department of Applied Mathematics and Theoretical Physics, University of Cambridge, Silver Street, Cambridge, CB3 9EW, UK

(Received 7 June 1999 and in revised form 19 May 2000)

The interaction between magnetic fields and convection is interesting both because of its astrophysical importance and because the nonlinear Lorentz force leads to an especially rich variety of behaviour. We present several sets of computational results for magnetoconvection in a square box, with periodic lateral boundary conditions, that show transitions from steady convection with an ordered planform through a regime with intermittent bursts to complicated spatiotemporal behaviour. The constraints imposed by the square lattice are relaxed as the aspect ratio is increased. In wide boxes we find a new regime, in which regions with strong fields are separated from regions with vigorous convection. We show also how considerations of symmetry and associated group theory can be used to explain the nature of these transitions and the sequence in which the relevant bifurcations occur.

1. Introduction

Stars like the Sun have deep outer convection zones and are magnetically active. Any attempt to explain the properties of their magnetic fields therefore requires an understanding of the interaction between those fields and convection. Observations reveal not only patterns of global activity, such as solar and stellar magnetic cycles, but also individual magnetic features, including sunspots and small-scale intergranular magnetic fields. Since the relevant parameter regimes are not accessible in the laboratory, these observations have motivated extensive theoretical studies of nonlinear magnetoconvection, which rely heavily on computation. The advent of powerful supercomputers, combined with high-resolution observations from the ground and from space, has at last made it possible to relate numerical results to fine-scale structures on the Sun (Title 2000). Computational studies have ranged from elaborate simulations of stellar convection and magnetoconvection to systematic numerical experiments with a range of idealized models. As time has advanced these models have progressed from two-dimensional Boussinesq to three-dimensional compressible configurations and so succeeded in reproducing many features that are actually observed. The calculations have also revealed a rich and fascinating variety of fluid dynamical behaviour.

Magnetoconvection, along with thermosolutal convection and other double-diffusive processes, leads to a great many different patterns of motion, some steady and

† Present address: School of Mathematical Sciences, University of Nottingham, University Park, Nottingham, NG7 2RD, UK.

https://doi.org/10.1017/S0022112000001373 Published online by Cambridge University Press

others time-dependent, and thus provides a marvellous testbed for nonlinear dynamics. The earlier two-dimensional problems generated complicated temporal behaviour with relatively simple spatial structures (Proctor & Weiss 1982; Hurlburt *et al.* 1989; Weiss *et al.* 1990; Proctor *et al.* 1994). In three dimensions there is the additional issue of pattern selection from the various competing planforms. Moreover, a systematic approach reveals transitions through different patterns as the system evolves from ordered motion (in a weakly nonlinear regime) to spatiotemporal chaos. The challenge then is to construct the underlying bifurcation structure that is associated with these transitions; it can only be met by identifying the symmetries that are broken.

This paper has three interlocking aims. Our main purpose is to explore transitions from order to disorder in the nonlinear regime and to understand the physical processes that are involved. To do this, we solve the governing equations in a square box with periodic lateral boundary conditions, and proceed by isolating specific patterns that are stable in small boxes and then expanding the box width so as to permit more complicated behaviour to occur. Thus our second aim is to discover how convective structures change when the aspect ratio (normalized width) is systematically increased. In order to describe this process we emphasize the spatiotemporal symmetries of different planforms and identify the sequences of symmetry-breaking bifurcations that lead to more complicated forms of behaviour. By identifying the relevant symmetry groups, together with their isotropy subgroups, it is possible to build up a consistent description of this process (cf. McKenzie 1988; Proctor & Weiss 1993). This taxonomic approach is an aid not only to recognizing solutions generated by nonlinear computations but also to predicting the existence of solutions that remain unstable. It can be underpinned by a more mathematical treatment of symmetry and symmetry-breaking bifurcations (Golubitsky, Stewart & Schaeffer 1988; Crawford & Knobloch 1991; Chossat & Lauterbach 2000). Our third aim is to explain the strengths and limitations of this approach, which is unfamiliar to many fluid dynamicists but necessary in order to understand our results. We hope that our brief survey may also prove useful in a wider context.

In a previous paper (Matthews, Proctor & Weiss 1995, henceforth referred to as Paper I) we considered three-dimensional behaviour in a shallow compressible layer (thereby breaking the up–down symmetry of Boussinesq magnetoconvection) and focused our attention on planforms for steady and oscillatory convection in mildly nonlinear regimes. The computations supplied examples of convection in rolls, squares and hexagons, together with travelling waves and alternating rolls, as well as streaming instabilities and pulsating waves. In stellar convection zones there are large variations with depth in properties such as density and (radiative) thermal diffusivity, and so it becomes appropriate to consider a layer that is deeper and more strongly stratified. Weiss *et al.* (1990) studied a range of two-dimensional behaviour as the superadiabatic gradient (measured by a dimensionless Rayleigh number R) was increased while the Chandrasekhar number Q (which measures the strength of the imposed magnetic field) was held constant. Such solutions are of course liable to be unstable to three-dimensional perturbations. For modelling solar magnetoconvection it is more appropriate to decrease Q for fixed R and Weiss *et al.* (1996) noted transitions from small-scale steady convection in strong magnetic fields to time-dependent behaviour and then to vigorous convection with broad chaotic plumes. Our aim here is to investigate the transitions between these different spatial patterns by increasing R for fixed Q (Proctor, Weiss & Matthews 1996), an approach that seems more natural in fluid dynamics.

To simplify the problem, we confine attention to a single underlying atmosphere

https://doi.org/10.1017/S0022112000001373 Published online by Cambridge University Press

(a polytrope with standard parameters), leaving three physical parameters to define the model system. These are Q, R and the ratio ζ of the magnetic diffusivity η to the thermal diffusivity κ. The last is significant since, for Q sufficiently large, convection typically sets in at an oscillatory (Hopf) bifurcation when $\zeta \ll 1$ but at a stationary (pitchfork) bifurcation when $\zeta \gg 1$. In our problem κ is inversely proportional to the density, which varies by an order of magnitude across the layer. We therefore define ζ at the middle of the layer in the static atmosphere and set the product $\zeta Q = 1200$ so that the imposed field strength is independent of ζ for a given value of R. In addition, there is a geometrical parameter, the aspect ratio λ, that defines the computational region.

The structure of the paper is as follows. The next section presents the model system and summarizes its linear stability. The nonlinear regime reveals a bewildering variety of patterns and it is essential to provide a framework within which they can be described. In § 3 we enumerate the most important planforms, together with their symmetries and group properties. This account is extended in the Appendix, where we describe the most relevant symmetry-breaking bifurcations and present some key aspects of representation theory and equivariant bifurcation theory.

For reference, we need to know what forms convection takes in the kinematic regime, when forces exerted by the magnetic field are negligible (cf. Busse & Clever 1998; Busse & Müller 1998); these solutions, which show transitions from two-dimensional rolls through wavy instabilities to large-scale three-dimensional plumes, are described in § 4. In subsequent sections we consider fields that are dynamically important and exhibit patterns of motion that are much more complicated. Our aim is not simply to display these patterns but rather to explain the sequences of transitions that lead from one planform to another and from order into chaos. To do so we first have to recognize the symmetries of each solution and so to identify its spatiotemporal symmetry group. That allows us to describe the symmetry-breaking bifurcations and hence to construct an appropriate bifurcation diagram, including solutions that are unstable.

We follow the treatment of the two-dimensional problem (Weiss *et al.* 1990) by considering three cases, with $\zeta = 0.6, 1.2$ and 6. Most of our attention is focused on the intermediate case with $\zeta = 1.2$ in mid-layer, which we present in § 5: this is the astrophysically relevant situation, with oscillations favoured near the top and overturning convection at the bottom. First we describe behaviour in a narrow box, with $\lambda = \frac{4}{3}$. Normally one expects the complexity of solutions to increase with increasing R but here the stringent geometrical constraint produces an unexpected transition from three-dimensional squares to two-dimensional rolls. The solutions found for $\lambda = 2$ are quite different. After the initial stationary bifurcation, resonant interactions lead to the appearance of a deformed hexagonal pattern; as R is increased, the pattern develops by way of intermittent bursts into chaotic plumes. This transition persists as λ is increased from 2 to $\frac{8}{3}$ and then to 4. So this behaviour is robust, although it does become more vigorously time-dependent in wider boxes. In § 5.4 we describe a different effect that appears when $\lambda = 8$, as reported by Tao *et al.* (1998). Long-wavelength modulation allows magnetic flux to separate from the motion, giving regions with strong fields and small-scale convection, and clusters of large plumes in regions that are almost field-free.

Next we turn to the case when $\zeta = 0.6$ and there is a Hopf bifurcation from the trivial solution: the results for $\lambda = 2$ in § 6 exhibit a variety of planforms. Once again, there is a transition through more complicated intermittent bursts to large-scale plumes. Thus bursting appears to characterize the transition from a magnetically

https://doi.org/10.1017/S0022112000001373 Published online by Cambridge University Press

dominated regime to one where the Lorentz force is only locally significant. Knobloch & Moehlis (1999) describe a variety of mechanisms that can lead to bursts and examples arise in several different fluid systems. The last case, in § 7, has $\zeta = 6$ so that $\eta \geqslant \kappa$ everywhere and convection sets in at a stationary bifurcation. As R is increased for $\lambda = 2$ there is a transition from rolls to squares, which co-exist with a particular form of periodic oscillation ('wobblers') and then give way to three-dimensional travelling waves, which eventually develop into large chaotic plumes. The squares are replaced by intermittent hexagonal patterns when the aspect ratio is increased.

In the concluding section we emphasize both the constraints imposed by the square lattice on the symmetries that are involved and the effects of finite aspect ratios on the structures that appear. Then we compare the patterns we describe with those found in other related calculations and in various fluid dynamical experiments. Finally, we relate these results to solar magnetic fields.

2. The model problem

We consider a plane layer of depth d, referred to Cartesian axes (x, y, z) with the z-axis pointing downwards, containing a perfect monatomic gas. The electrical and thermal conductivities, the shear viscosity, the specific heats at constant density and pressure, and the magnetic permeability are all assumed to be constant. The upper and lower boundaries are held at fixed temperatures T_0 and $T_0 + \Delta T$, respectively, and, in the absence of any motion, there is an imposed magnetic field $\boldsymbol{B}_0$ that is uniform and vertical. Then there is a uniformly stratified equilibrium solution (the reference atmosphere) corresponding to a polytrope of index m. If the origin is chosen so that $z = 0$ at the top of the layer, the temperature $T(z)$, the density $\rho(z)$ and the pressure $P(z)$ are given by

$$T(z) = T_0(1 + \theta z/d), \quad \rho(z) = \rho_0(1 + \theta z/d)^m, \quad P(z) = R_* T_0 \rho_0 (1 + \theta z/d)^{m+1}, \quad (2.1)$$

where $\theta = \Delta T/T_0$, $\rho_0 = \rho(0)$ and R_* is the gas constant. For our model we adopt the standard reference atmosphere with $m = 1$ and $\theta = 10$ that has been used in previous studies of stratified magnetoconvection (Hurlburt & Toomre 1988; Weiss *et al.* 1990, 1996) as well as in several related investigations (e.g. Cattaneo *et al.* 1991). Thus the model problem differs from that treated in Paper I in that the layer is much more strongly stratified. We shall also be carrying out a more ambitious survey, advancing further into the nonlinear regime and studying behaviour in larger boxes as the aspect ratio is increased.

As in Paper I, we scale lengths with the layer depth d, density with ρ_0, temperature with T_0, magnetic fields with B_0 and time with the reduced acoustic travel time $d/\sqrt{R_* T_0}$. Note that this scaling for time differs by a factor of $\sqrt{\Delta T/T_0}$ from that used in an astrophysical context by Weiss *et al.* (1990, 1996), Tao *et al.* (1998) and Blanchflower, Rucklidge & Weiss (1998). To prescribe the state of the system we introduce a dimensionless thermal diffusivity κ and F, the square of the ratio of the Alfvén speed to the isothermal sound speed at the upper boundary. The Rayleigh number R, the ratio β of the gas pressure to the magnetic pressure and the diffusivity ratio ζ are all defined at the middle of the layer ($z = \frac{1}{2}$). With our reference atmosphere

$$R = 240/\sigma\kappa^2, \quad \beta = 72/F, \quad (2.2)$$

where the Prandtl number σ does not depend on z. We choose to measure the

https://doi.org/10.1017/S0022112000001373 Published online by Cambridge University Press

magnetic field strength in terms of the Chandrasekhar number

$$Q = 6F/\sigma\zeta\kappa^2 = 9R/5\beta\zeta = RF/40\zeta. \tag{2.3}$$

Note therefore that $F \propto 1/R$ when R is varied for fixed Q.

The evolution of the velocity $\boldsymbol{u}$ and the magnetic field $\boldsymbol{B}$, together with ρ, T and P, is then governed by equations (2.4)–(2.9) of Paper I. These equations are solved in the region $\{0 \leqslant x \leqslant \lambda; 0 \leqslant y \leqslant \lambda; 0 \leqslant z \leqslant 1\}$, with periodic boundary conditions in the x- and y-directions. At the top and bottom of the layer standard free boundary conditions are imposed: the temperature is fixed so that $T(x, y, 0) = 1$, $T(x, y, 1) = 1 + \theta = 11$ and the magnetic field is constrained to be vertical, while the vertical velocity and the tangential components of the viscous stress all vanish, so that

$$B_x = B_y = \partial B_z/\partial z = u_z = \partial u_x/\partial z = \partial u_y/\partial z = 0 \quad \text{at} \quad z = 0, 1. \tag{2.4}$$

Blanchflower *et al.* (1998) have investigated the effects of introducing a radiative boundary condition and matching $\boldsymbol{B}$ to a potential field at $z = 0$. They found that altering the boundary conditions in a two-dimensional version of this problem shifted bifurcation points but made no qualitative difference to the bifurcation sequence.

Our system possesses a trivial static solution with $\boldsymbol{u} = 0$, $\boldsymbol{B} = \hat{\boldsymbol{z}}$ and $T = \rho = 1 + \theta z$, so that the density increases by a factor of eleven across the layer. Since the local value of the diffusivity ratio is proportional to the density it increases from $\zeta/6$ at the top of the layer to $11\zeta/6$ at its base. If U is a typical dimensionless velocity then the Reynolds number Re at the top of the layer and the magnetic Reynolds number Rm are given by

$$Re = \frac{U}{\sigma\kappa} = U\left(\frac{R}{240\sigma}\right)^{1/2}, \quad Rm = \frac{6U}{\zeta\kappa} = \frac{U}{\zeta}\left(\frac{3R}{20}\right)^{1/2}. \tag{2.5}$$

Following the choice of parameters for the two-dimensional problem (Weiss *et al.* 1990), we set the Prandtl number $\sigma = 1$ and fix the product $\zeta Q = 1200$. Then we compare results for three different values of the mid-layer diffusivity ratio.

The stability of the trivial solution is determined by linearizing the governing equations and calculating the growth rates of eigenfunctions that are proportional to $\exp \mathrm{i}(k_x x + k_y y)$. These growth rates depend only on the horizontal wavenumber $k = (k_x^2 + k_y^2)^{1/2}$, so that, for instance, large squares and transverse rolls (both with $k = 2\pi/\lambda$ – see § 3.1 below) become unstable at the same value of R, while small squares and diagonal rolls (with $k = 2\sqrt{2}\pi/\lambda$) become unstable together at another value. Only a nonlinear analysis can establish which of the two planforms is preferred at each bifurcation point. In figure 1 we show the values of R at the pitchfork bifurcation ($R^{(\mathrm{e})}$) and, where appropriate, at the Hopf bifurcation ($R^{(\mathrm{o})}$) as functions of k/π for the three cases $\zeta = 6$, 1.2 and 0.6. When $\zeta = 6$, $R^{(\mathrm{e})}$ attains its minimum value $R_{\mathrm{c}}^{(\mathrm{e})} = 7910$ for a wavenumber $k_{\mathrm{c}} = 1.54\pi$; when $\zeta = 1.2$ – the astrophysically relevant case – there is still only a stationary bifurcation, with $R_{\mathrm{c}}^{(\mathrm{e})} = 28\,200$ and $k_{\mathrm{c}} = 2.10\pi$; with $\zeta = 0.6$, however, convection sets in at an oscillatory bifurcation with $R_{\mathrm{c}}^{(\mathrm{o})} = 29\,800$ and $k_{\mathrm{c}} = 1.50\pi$ again.

In §§ 4–8 we investigate nonlinear behaviour in square boxes that are large enough to accommodate modes with k close to k_{c}. The nonlinear solutions have to be obtained numerically and we use the mixed finite difference/pseudospectral code described in Paper I. For numerical experiments with $\lambda = 2$ we achieve sufficient accuracy with a resolution of 32 points (16 complex Fourier modes) in each of the x- and y-directions, and 40 mesh intervals (41 points) in the z-direction; where greater precision is needed

https://doi.org/10.1017/S0022112000001373 Published online by Cambridge University Press

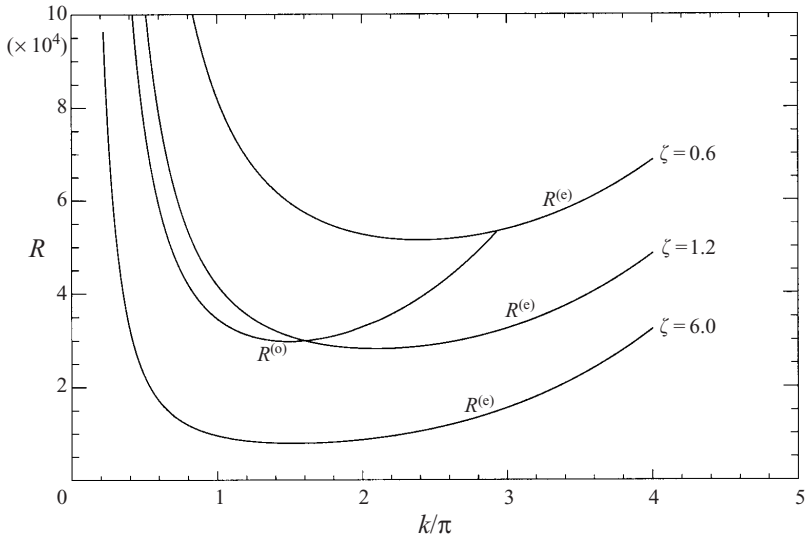


FIGURE 1. Linear theory: $R^{(e)}$ and $R^{(o)}$ as functions of the wavenumber k/π for $\zeta = 6$, 1.2 and 0.6. (After Weiss *et al.* 1990.)

the mesh is refined to $48 \times 48 \times 61$. Most of our calculations were carried out using Sun, Hewlett-Packard, Silicon Graphics and DEC workstations. The runs with $\lambda = 4$ and $\lambda = 8$ used 64 nodes on a Hitachi SR-2201 massively parallel supercomputer, with up to 256 points in the x- and y-directions.

3. Planforms and their symmetries

Throughout this paper, we shall be concerned with describing transitions between different patterns of fluid motion. Regular structures in cellular convection, like crystals, can be classified by specifying the group of symmetries (reflections, rotations, and translations) that leave the pattern invariant (cf. McKenzie 1988). Patterns of convection are often time-dependent, and this necessitates combining spatial symmetries with a shift in time so as to form new spatiotemporal symmetry groups.

These difficulties have been tackled in two ways. An elementary approach was put forward by Proctor & Weiss (1993) in order to analyse transitions that occur in two-dimensional magnetoconvection. Their technique was based on the observation, appropriate for the range of problems they studied, that when a pattern loses stability and breaks some of its symmetries, half of the original symmetries are broken and half are retained. By introducing a 'half-period time shift' symmetry, they were able to describe transitions from steady to time-dependent behaviour, and to classify the spatiotemporal symmetries of the new time-dependent solutions.

This straightforward and remarkably successful approach is easy to apply in simple situations. Unfortunately, however, it can only describe a limited range of transitions in three-dimensional convection, and a more general method is needed. Such a method, called equivariant bifurcation theory (cf. Golubitsky *et al.* 1988; Crawford & Knobloch 1991), is widely used in the nonlinear dynamics community, but is less well known in the fluid mechanics literature, in part because of the mathematical technicalities of group theory that are required. Equivariant bifurcation theory is a powerful technique, capable of explaining a much wider range of phenomena than

https://doi.org/10.1017/S0022112000001373 Published online by Cambridge University Press

occurs in the present paper; in the Appendix we extract and explain those aspects that we require. As a prelude to equivariant bifurcation theory, the Appendix discusses aspects of group representation theory; this classifies the relations between patterns and their symmetries. The material in the Appendix, though somewhat technical, turns out to be invaluable in the analysis of the behaviour seen in numerical simulations of the PDEs. In particular, these methods were used in the construction of the bifurcation diagrams in figures 5 and 13. Such bifurcation diagrams show in what range of parameters a particular type of solution might be found, whether or not it is stable, and what else might be found if it becomes unstable. If a particular transition has been observed, for example from one pattern of convection to another, we can determine whether the transition could have happened in a single step (or whether an intermediate pattern might be required), and also whether or not other, perhaps unstable, patterns might have been created at the same bifurcation point. At first glance, unstable patterns might appear to be uninteresting as they cannot be observed directly in an experiment, but they are important for a number of reasons: first, they might become stable at other parameter values; second, they might be only weakly unstable, and so show up in a transient; and third, unstable patterns are implicated in the bursting phenomenon, when the system repeatedly loses symmetries and then regains them. All three of these effects are found in the calculations we describe.

3.1. *Symmetries of plumes on a square lattice*

It is essential to understand the symmetries of a solution before its possible modes of instability can be determined. In this section we give a brief description of the groups we shall encounter. The transitions between them are analysed in the Appendix. Since we are concerned here with three-dimensional convection in a strongly stratified layer, the only relevant spatial symmetries are those that correspond to the arrangement of rising (or sinking) plumes or sheets in the (x, y)-plane. Before we proceed, it may be helpful to recall some elementary properties of symmetry groups. A single symmetry operation i that is its own inverse (for example, 180° rotation about a vertical axis) generates the group $\{E, i\}$, where E is the identity. This group is called Z_2. A rectangle possesses three symmetries: the 180° rotation i as well as m_x and m_y, corresponding to reflections about two orthogonal planes, normal to the x- and y-axes, respectively, so the symmetry group (called D_2) is $\{E, m_x, m_y, i\}$. Note that the point symmetry $i = m_x m_y = m_y m_x$. A square has these four symmetries as well as four more: m_d and $m_{d'}$, corresponding to reflection about the two diagonals, and ρ and ρ^3, corresponding to 90° and 270° degree rotations about the centre, so its symmetry group (called D_4) is

$$\{E, m_x, m_y, m_d, m_{d'}, \rho, i, \rho^3\}. \tag{3.1}$$

This group has as one of its subgroups the cyclic group of four elements, Z_4, given in this case by $\{E, \rho, i, \rho^3\}$. The groups D_2 and Z_4 each have four elements but they are not equivalent, since Z_4, unlike D_2, has two elements (ρ, ρ^3) of order 4.

We shall use the names Z_2, D_2 etc. to describe the structure of a group, so, for example, D_2 has three subgroups $\{E, m_x\}$, $\{E, m_y\}$ and $\{E, i\}$ that are all different, but which are all isomorphic to Z_2. In addition, D_2 can be generated by combining any two of these three Z_2 subgroups, so we write $D_2 = Z_2 \otimes Z_2$, where $\otimes$ indicates the direct product of the groups, used when each element of either group commutes with every element of the other group.

These simple groups are the building blocks out of which we construct the symmetry groups required to describe patterns of convection. In general, the group Z_n can be thought of geometrically as the n-element rotational symmetry group of a regular

https://doi.org/10.1017/S0022112000001373 Published online by Cambridge University Press

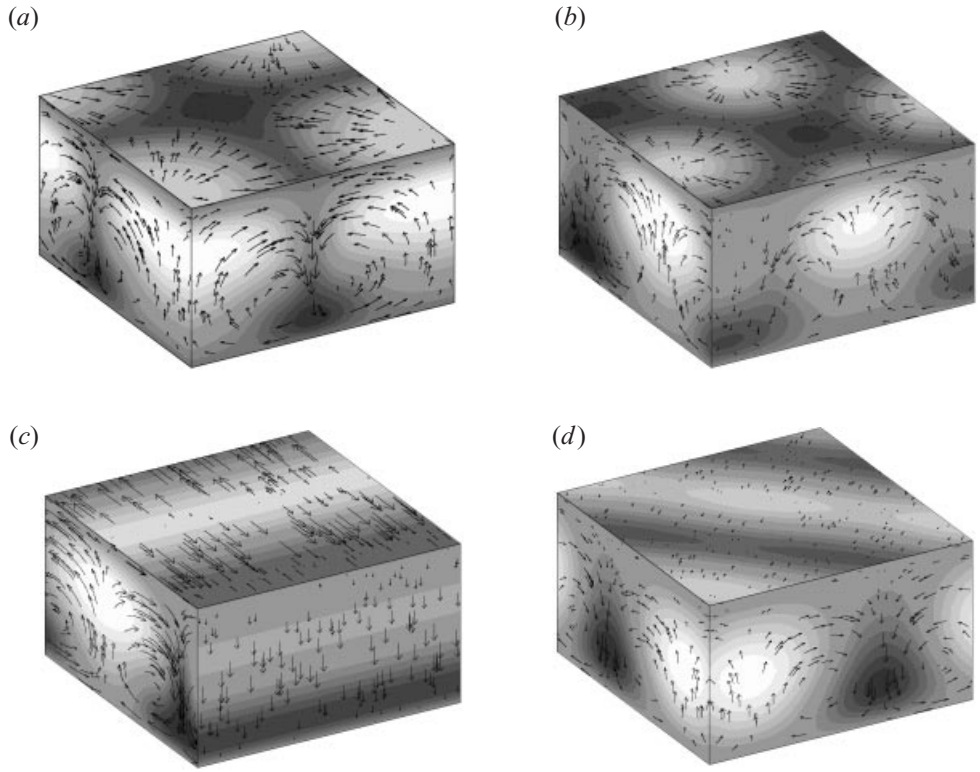


FIGURE 2. Three-dimensional nonlinear solutions in square boxes: (*a*) Large squares ($Q = 200$, $\zeta = 6$, $R = 30\,000$); (*b*) small squares ($Q = 200$, $\zeta = 6$, $R = 20\,000$); (*c*) transverse rolls ($Q = 0$, $R = 5\,000$); (*d*) diagonal rolls ($Q = 200$, $\zeta = 6$, $R = 10\,000$). Each panel depicts behaviour on the boundaries of the computational box. The shading of the sidewalls indicates relative temperature fluctuations and the arrows represent tangential velocity components. Here the shading at the top and base correspond to the vertical temperature gradient.

n-gon, without reflections, while D_n has the rotational symmetries of Z_n combined with a reflection, and so has $2n$ elements. Other groups we shall require are $D_{2h} = D_2 \otimes Z_2$, the 8-element symmetry group of a rectangular prism, and $D_{4h} = D_4 \otimes Z_2$, the 16-element symmetry group of a square prism.

We illustrate these symmetry groups with reference to the convective patterns displayed in figure 2. Here the grey-scale shading represents relative temperature fluctuations on the sidewalls of the box, and the vertical temperature gradient on the upper bounding surface. The superposed arrows indicate the direction and magnitude of the tangential components of the velocity. The pattern in figure 2(*a*), which we call large squares, has a single upward (and downward) plume in each cell and has the D_4 symmetry of a square centred on some point (x_0, y_0), such that $0 < x_0, y_0 \leqslant \frac{1}{2}\lambda$, where $\rho : (x, y) \to (x_0 + y_0 - y, x - x_0 + y_0)$ corresponds to rotation by 90° about (x_0, y_0), $m_x : (x, y) \to (2x_0 - x, y)$ is the reflection in the plane $x = x_0$ and $m_y : (x, y) \to (x, 2y_0 - y)$ is the reflection in the plane $y = y_0$. Figure 2(*b*) shows small squares, which have two upward (and downward) plumes within the box; this pattern has D_4 symmetry but is in addition invariant under the translation symmetry $\tau : (x, y) \to (x + \frac{1}{2}\lambda, y + \frac{1}{2}\lambda)$ that moves the pattern by $\frac{1}{2}\lambda$ in the x- and y-directions, taking one upward plume to the other. Combining the rotations and reflections of D_4 with the translation τ (which generates the group Z_2) results in the group D_{4h}.

https://doi.org/10.1017/S0022112000001373 Published online by Cambridge University Press

We turn now to continuous translation symmetries, which do not have analogues in crystal structure. The initial trivial state, in which there is no motion, has D_4 symmetry arising from the square plan of the box, but it is also unchanged by any horizontal translation, since we use periodic lateral boundary conditions. However, shifting in space by a distance λ in the x- or y-directions will leave any pattern unchanged, so these translations act as the identity. Any pattern occupying the box will have symmetries that form a subgroup of the product of D_4 and this group of translations.

As an example, transverse rolls (figure 2*c*) are unchanged after reflecting in the x-direction or in the y-direction, and after translating by any amount in the y-direction. Combining the y-reflection with the y-translations gives us the symmetry group $O(2)$ of a circle under rotations and reflections, so the symmetry group of rolls is $Z_2 \otimes O(2)$. There is also a second solution with orthogonally oriented rolls.

Similarly, diagonal rolls (figure 2*d*) have the diagonal reflection symmetry $m_{d'}$: $(x, y) \to (x_0 + y_0 - y, x_0 + y_0 - x)$ about the plane separating the pair of rolls, and the $O(2)$ symmetry of translations and reflections ($m_d : (x, y) \to (x_0 - y_0 + y, y_0 - x_0 + x)$) along the axis of the rolls; they also have the symmetry τ, so their symmetry group is $Z_2 \otimes O(2) \otimes Z_2 = D_2 \otimes O(2)$.

The patterns described here could be formed in primary instabilities of the trivial solution (with different wavenumbers and critical Rayleigh numbers). The transverse roll (figure 2*c*) can be combined with its 90° rotation to give large squares (figure 2*a*), while the two sets of diagonal rolls (figure 2*d* and its 90° rotation) yield the small squares of figure 2(*b*). At onset, the patterns in figures 2(*a*) and 2(*c*) both have the same wavenumber $k = 2\pi/\lambda$, while those in figures 2(*b*) and 2(*d*) have wavenumber $k = 2\sqrt{2}\pi/\lambda$. Similarly, there are patterns of narrow rolls (not illustrated, but like transverse rolls with half the wavelength), each with one of the additional symmetries $m'_x : (x, y) \to (2x_0 - \frac{1}{2}\lambda - x, y)$, $m'_y : (x, y) \to (x, 2y_0 - \frac{1}{2}\lambda - y)$, and tiny squares, all with wavenumber $k = 4\pi/\lambda$.

Finally, steady patterns are unchanged by any translation in time, but if time-dependence is introduced through a Hopf bifurcation the new oscillatory solutions will be periodic in time, with period Π. With this periodic time-dependence in mind, we regard the steady solutions as invariant under a continuous symmetry S^1, the symmetry group of a circle under rotations. Thus squares and rolls have $D_4 \otimes S^1$ and $Z_2 \otimes O(2) \otimes S^1$ spatiotemporal symmetries, respectively.

The spatial symmetries of rolls or squares may be broken in secondary bifurcations, which are described in the Appendix. For instance, there is a pitchfork bifurcation from steady transverse rolls that leads to varicose rolls (Hirschberg & Knobloch 1993) with the reflection symmetries m_x and m_y; similarly, breaking the 90° rotational symmetry of a square in a pitchfork bifurcation gives a pair of solutions with the same reflection symmetries. These two solutions may look different but they possess the same D_2 spatial symmetry; in fact they may form a continuous family linking rolls to squares (cf. figure 13*a* below).

To take a more complicated example, involving oscillatory bifurcations, travelling squares may appear either in a primary Hopf bifurcation (Silber & Knobloch 1991; Clune & Knobloch 1994) or in a secondary pitchfork from steady squares, as in figure 5(*a*) below (Rucklidge 1997). Similarly, travelling varicose rolls may appear after a symmetry-breaking Hopf bifurcation from rolls or, alternatively, after a pitchfork from varicose rolls – either with the varicosity travelling parallel to the rolls or with the rolls travelling in the perpendicular direction. Yet all four cases have the same Z_2 reflection symmetry, demonstrating again that, on a branch of solutions (defined by symmetry) the solutions may – and indeed often do – look very different at either end.

https://doi.org/10.1017/S0022112000001373 Published online by Cambridge University Press

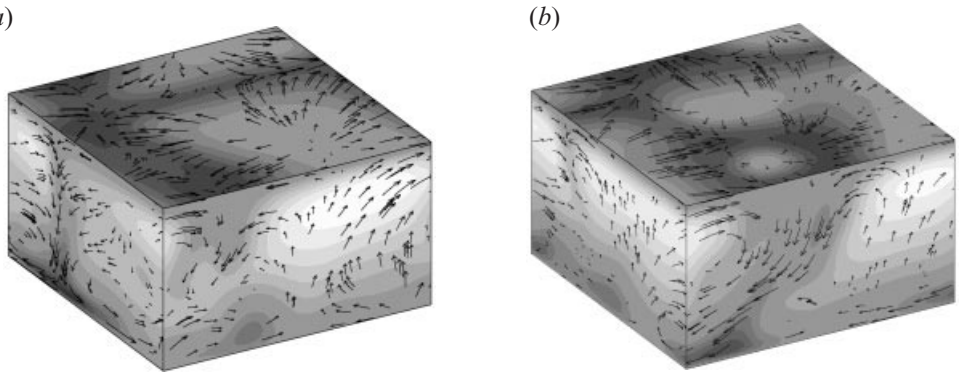


FIGURE 3. Three-dimensional solutions in the kinematic regime. As for figure 2, showing chaotic plumes for $Q = 0$ and $R = 40\,000$. (*a*) $t = 66$, (*b*) $t = 73$.

R	Mesh	$\langle u^2\rangle^{1/2}$	Figure	Type of solution
1 000	$32^2 \times 41$	0.00		Motion decays
2 000	$32^2 \times 41$	0.34		Steady transverse rolls
5 000	$32^2 \times 41$	0.55	2(*c*)	Steady transverse rolls
10 000	$48^2 \times 61$	0.64		Oscillatory instability of rolls
20 000	$48^2 \times 61$	0.65		Aperiodic modulation
30 000	$48^2 \times 61$	0.68		Aperiodic (single plume)
40 000	$48^2 \times 61$	0.70	3(*a*, *b*)	Aperiodic (large-scale plumes)

TABLE 1. Nonlinear runs: $Q = 0$, $\lambda = 2$.

4. The kinematic regime ($Q = 0$)

We begin by describing nonlinear behaviour in the absence of a magnetic field. The velocity and temperature are then indistinguishable from those in the kinematic limit, when the Lorentz force has no dynamical effect. Unless dynamo action occurs (cf. Cattaneo 1999), we expect that for any finite value of Q the pattern of convection will come to resemble that in the field-free case when R is sufficiently large. In order to recognize when this happens we therefore need to establish the form of solutions in the kinematic regime.

When $Q = 0$ convection sets in at a stationary bifurcation. For our reference atmosphere the critical Rayleigh number $R_c^{(e)} = 1190$ and the corresponding wavenumber $k_c = 0.77\pi$ (Gough *et al.* 1976). That would correspond to an aspect ratio $\lambda = 2.6$, which is somewhat larger than the value $\lambda = 2$ that we adopt for our computations. The nonlinear results are summarized in table 1, which includes the r.m.s. velocity $\langle u^2\rangle^{1/2}$, averaged over space and time, as a measure of the vigour of convection. Transverse rolls, with a basic wavenumber $k = \pi$, are initially preferred and the solution for $R = 5\,000$, which is illustrated in figure 2(*c*), possesses $Z_2 \otimes O(2)$ symmetry. As R is increased there is a secondary Hopf bifurcation and the rolls develop an oscillatory instability, just as they do in Boussinesq convection (Busse 1972; Meneguzzi *et al.* 1987; Croquette & Williams 1989). For our choice of aspect ratio this develops into a finite-amplitude periodic standing wave at $R = 10\,000$.

As R is further increased the oscillatory modulation grows more violent until convection becomes completely three-dimensional and aperiodic. Figure 3 shows the

https://doi.org/10.1017/S0022112000001373 Published online by Cambridge University Press

pattern for $R = 40\,000$. The rolls have entirely disappeared and motion is dominated by broad rising plumes whose width is limited by the size of the computational box. Owing to the stratification these plumes expand rapidly as they impinge upon the upper boundary. They are enclosed by a network of sinking fluid and the peak speeds are in the downward flow. This pattern, which evolves continuously and is apparently chaotic, is typical of highly nonlinear convection in a strongly stratified layer and has been reproduced in various numerical experiments (e.g. Cattaneo *et al.* 1991).

5. The transition from order to disorder ($\zeta = 1.2$)

Imposing a magnetic field allows a much greater variety of behaviour. In this section we investigate nonlinear convection with $Q = 1\,000$ and $\zeta = 1.2$, so that the diffusivity ratio increases from 0.2 at the top of the layer to 2.2 at the bottom. (This choice is motivated by behaviour in the Sun: $\zeta \ll 1$ throughout most of its interior, owing to the efficiency of radiative transfer, but ionization of hydrogen and helium increases the opacity and decreases the radiative diffusivity, so that $\zeta > 1$ at depths of 2 000–20 000 km below the photosphere.) Although $\zeta < 1$ at the top of the box, steady behaviour is initially preferred, and strong fields require narrower cells at onset than in the field-free case. From figure 1, convection sets in at a stationary bifurcation with $R_c^{(e)} = 28\,200$ and $k_c = 2.10\pi$. In the weakly nonlinear regime we might therefore expect to obtain steady solutions with transverse rolls or large squares in a box with $\lambda \approx 1$.

5.1. *Spatially modulated oscillations in a narrow box* $\left(\lambda = \frac{4}{3}\right)$

Weiss *et al.* (1990) studied the two-dimensional problem with $\lambda = \frac{4}{3}$. The initial bifurcation led to steady convection with a pair of rolls in the box but as R was increased countercells appeared and grew until the solution became periodic, with four spatially modulated rolls. So we begin by investigating three-dimensional behaviour with the same value of λ. After presenting the computational results we describe the symmetries of the numerical solutions and then establish the underlying bifurcation structure.

Table 2 lists the relevant runs. The values of $\langle u^2 \rangle^{1/2}$ can be used to calculate a magnetic Reynolds number Rm from equation (2.5). Convection sets in as a steady pattern of small squares with $k = 2.12\pi$, which is initially stable. At $R = 50\,000$ we obtain travelling small squares which drift very slowly parallel to the x- or y-axis. By $R = 60\,000$ there are modulated travelling squares, with adjacent plumes that pulsate periodically in antiphase with each other as they drift. As R is raised the modulation increases in amplitude while the drift velocity declines until, at $R = 70\,000$, there are stationary oscillations with nearest neighbours pulsating vigorously in alternation. Such spatially modulated oscillations are a characteristic feature of the transition from steady to time-dependent behaviour but they appear most prominently with this aspect ratio. In figures 4(a) and 4(b) we illustrate two opposite phases of this periodic oscillation, now using the grey-scale to denote the variation of B^2 on the upper boundary (light regions correspond to high values of B^2). Note that the x- and y-directions are not equivalent and that the plumes are elongated in one of these directions only. As R is increased this elongation becomes more pronounced until at $R = 100\,000$ we only find two-dimensional spatially modulated rolls, as illustrated in figures 4(c) and 4(d) (cf. Weiss *et al.* 1996). In these solutions adjacent plumes wax and wane alternately in strength, so that the velocity reverses at the top of the layer but not at its base. The two-dimensional rolls are unstable to three-dimensional

https://doi.org/10.1017/S0022112000001373 Published online by Cambridge University Press

R	Mesh	$\langle u^2\rangle^{1/2}$	Figure	Type of solution
37 000	$24^2 \times 33$	0.08		Small squares
40 000	$24^2 \times 33$	0.10		Small squares
45 000	$24^2 \times 33$	0.10		Small squares
50 000	$32^2 \times 41$	0.14		Travelling small squares
55 000	$24^2 \times 33$	0.15		Travelling small squares
60 000	$24^2 \times 33$	0.17		Modulated travelling small squares
60 000	$32^2 \times 41$	0.17		Modulated travelling small squares
65 000	$24^2 \times 33$	0.19		Modulated travelling small squares
70 000	$24^2 \times 33$	0.22		Spatially modulated asymmetric squares
80 000	$24^2 \times 33$	0.23		Spatially modulated asymmetric squares
80 000	$32^2 \times 41$	0.23	4(a, b)	Spatially modulated asymmetric squares (from two-dimensional rolls)
85 000	$24^2 \times 33$	0.24		Spatially modulated asymmetric squares
90 000	$24^2 \times 33$	0.24		Spatially modulated rolls (from asymmetric squares)
90 000	$32^2 \times 41$	0.24		Spatially modulated varicose rolls (from asymmetric squares)
90 000	$32^2 \times 41$	0.24		Spatially modulated rolls (from rolls)
100 000	$24^2 \times 33$	0.25		Spatially modulated rolls (from asymmetric squares)
100 000	$32^2 \times 41$	0.26	4(c, d)	Spatially modulated rolls (from asymmetric squares)
120 000	$32^2 \times 41$	0.27		Spatially modulated rolls (from rolls)
140 000	$32^2 \times 41$	0.32		three-dimensional and chaotic (from rolls)

TABLE 2. Nonlinear runs: $\zeta = 1.2$, $Q = 1\,000$, $\lambda = \frac{4}{3}$. Note comparison between different meshes.

perturbations when $R = 80\,000$ but both two-dimensional and three-dimensional oscillations are stable for $R = 90\,000$.

The two-dimensional spatially modulated oscillations are identical with solutions found by Weiss *et al.* (1990) for a system that was constrained to be two-dimensional. They conjectured that three-dimensional oscillations would be preferred if that constraint were removed (as in, for example, figures 4*a* and 4*b*) – and certainly did not anticipate that the three-dimensional pattern would give way to two-dimensional rolls as the Rayleigh number was increased. In fact the rolls remain stable at $R = 120\,000$ but do finally become unstable to three-dimensional perturbations when $R = 140\,000$. This sequence, with squares giving way to rolls, is quite different from the patterns found below with larger aspect ratios. When λ is too small the system apparently prefers a two-dimensional pattern and achieves a larger effective wavenumber in the nonlinear regime.

The power of the group-theoretic approach becomes apparent when we attempt to establish the underlying bifurcation structure. The first stage is to clarify the symmetries of the various patterns that are involved. As R is increased the first bifurcation from the trivial solution gives rise to diagonal rolls and small squares ($k = 2.12\pi$, $R^{(e)} = 28\,200$); this is followed by transverse rolls and large squares ($k = 1.5\pi$, $R^{(e)} = 30\,850$) and then by narrow transverse rolls and tiny squares ($k = 3\pi$, $R^{(e)} = 32\,530$). The steady small squares that are initially preferred have D_{4h} spatial symmetry. When steady convection gives way to travelling small squares, moving parallel to the y-axis (say), they only retain the symmetry $\{E, m_x, \tau, \tau m_x\} = D_2$ in the stationary frame; there is, however, a uniformly moving frame in which they are steady. The travelling small squares in turn undergo a Hopf bifurcation in which the translational symmetry τ is broken, leading to spatially mod-

https://doi.org/10.1017/S0022112000001373 Published online by Cambridge University Press

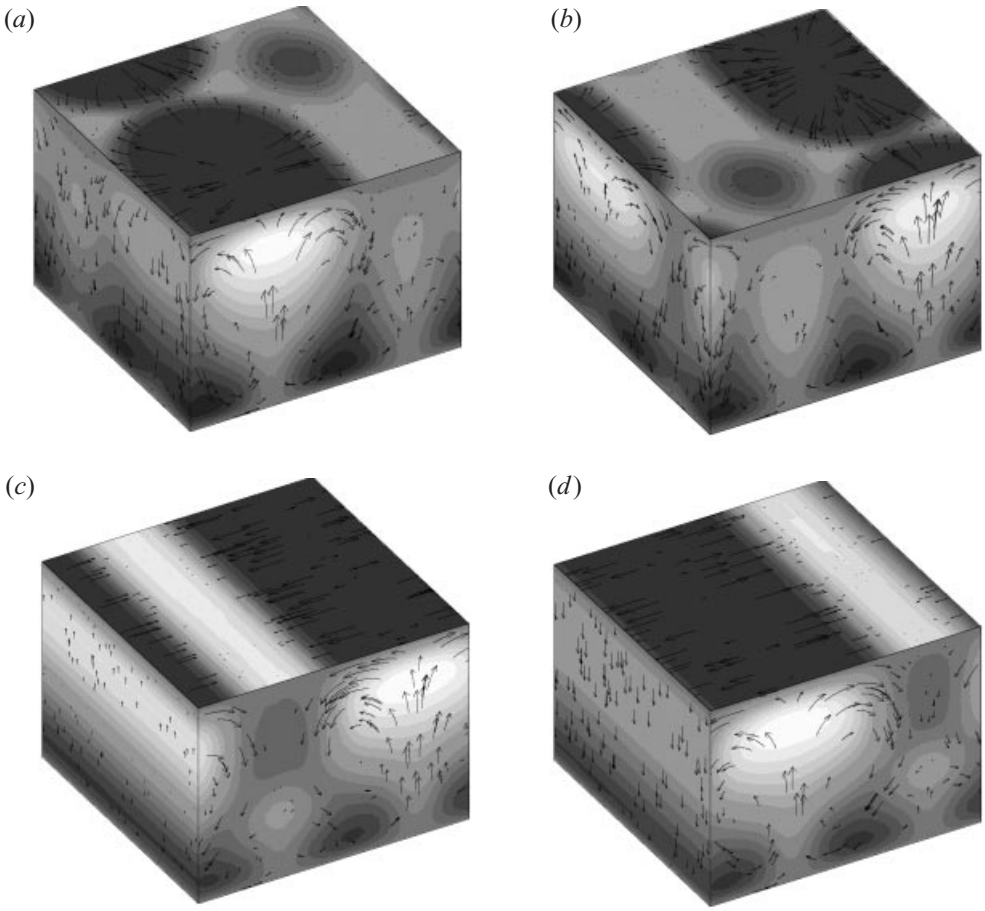


FIGURE 4. Geometrical constraints: behaviour in a narrow box. Three-dimensional solutions for $\zeta = 1.2$, $Q = 1\,000$, $\lambda = 4/3$: (a, b) spatially modulated asymmetric squares/varicose rolls ($R = 80\,000$); (c, d) spatially modulated two-dimensional rolls ($R = 100\,000$). As for figure 2, but here and henceforth with B^2 plotted at the top.

ulated travelling squares with period Π in the moving frame. To describe them we introduce the spatiotemporal symmetries $t_e : (x, y, z, t) \to (x, y, z, t + \frac{1}{2}\Pi)$ and $t_\tau = t_e\tau$ (cf. § A.1). Then their spatiotemporal symmetry group is $\{E, m_x, t_\tau, t_\tau m_x\} = D_2$ in the moving frame. After the next bifurcation the pattern acquires the symmetry m_y and the spatially modulated stationary solution in figures 4(*a*) and 4(*b*) has the spatiotemporal symmetry group $\{E, m_x, m_y, i, t_\tau, t_\tau m_x, t_\tau m_y, t_\tau i\} = D_{2h}$ in the stationary frame. This is the symmetry of spatially modulated varicose rolls and the plumes grow more and more elongated in the y-direction until the pattern gains $O(2)$ symmetry. The two-dimensional spatially modulated rolls then have the spatiotemporal symmetry $D_2 \otimes O(2)$.

Figure 5 shows a minimal bifurcation diagram for this problem. The initial bifurcation (a pitchfork) gives rise to supercritical branches of diagonal rolls and small squares, of which only the latter are stable. The next bifurcation (a pitchfork with D_{4h} symmetry, corresponding to a two-dimensional representation, as discussed in § A.2) gives rise to branches of travelling small squares moving in either direction

https://doi.org/10.1017/S0022112000001373 Published online by Cambridge University Press

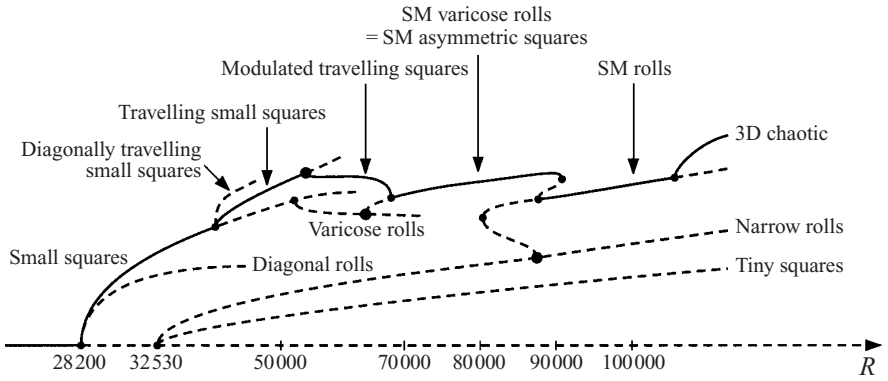


FIGURE 5. Schematic bifurcation diagram for the transition via spatially modulated (SM) behaviour to two-dimensional rolls in a narrow box ($\zeta = 1.2$, $Q = 1\,000$, $\lambda = \frac{4}{3}$). Small (large) filled circles indicate pitchfork (Hopf) bifurcations. Solid (broken) lines indicate stable (unstable) solutions.

parallel to the x-axis, the y-axis or either of the two diagonals. Of these, transversely travelling squares are preferred. There is then a Hopf bifurcation leading to spatially modulated travelling squares (which share the symmetry of spatially modulated travelling varicose rolls). To explain the origin of the branch of spatially modulated but stationary varicose rolls we presume that the unstable branch of steady small squares undergoes a tertiary bifurcation at which the D_{4h} spatial symmetry is broken (with a one-dimensional representation), producing a branch of steady solutions with the rectangular (D_2) spatial symmetry of simple varicose rolls and the translational symmetry τ; the spatial symmetry group is therefore D_{2h} again. Breaking the translational symmetry in a Hopf bifurcation (which could, alternatively, precede the breaking of D_{4h} symmetry) then yields a branch of spatially modulated varicose rolls, which gains stability from spatially modulated travelling squares in a supercritical pitchfork bifurcation. This stability is finally transferred to spatially modulated two-dimensional rolls in another pitchfork bifurcation.

The spatially modulated rolls are connected to a branch of narrow rolls that bifurcates from the trivial solution. Let us, for convenience, assume that transverse rolls are preferred to large squares and that narrow transverse rolls are preferred to tiny squares. Then spatially modulated rolls develop within an invariant subspace with $O(2)$ symmetry. In this subspace there is a pitchfork bifurcation giving rise to narrow transverse rolls. They subsequently undergo a subcritical Hopf bifurcation that produces spatially modulated rolls, which in turn acquire stability in a saddle-node bifurcation, as shown in figure 5.

Note that the unstable branches may well be adorned with further bifurcations, as in the model problem discussed by Moore & Weiss (2000), provided that those bifurcations do not affect the stability of the solutions that are observed. There are also other branches bifurcating from the trivial solution. Figure 5 does not include the branch of transverse rolls (with $k = 1.5\pi$) that lies between the two branches with $k = 2.12\pi$ and $k = 3\pi$. Fortunately, the connections between that branch and the branch of narrow transverse rolls have already been explored by Weiss *et al.* (1990 – see figure 9*b*). Thus the bifurcation diagram needs to be augmented by adding those details to the figure.

https://doi.org/10.1017/S0022112000001373 Published online by Cambridge University Press

R	Mesh	$\langle u^2\rangle^{1/2}$	Figure	Type of solution
30 000	$32^2 \times 41$	0.05		Irregular hexagons (4 plumes)
40 000	$32^2 \times 41$	0.12	6(*a*)	Irregular hexagons (4 plumes)
60 000	$32^2 \times 41$	0.17	6(*b*)	Asymmetric irregular hexagons
65 000	$32^2 \times 41$	0.18		Asymmetric irregular hexagons
70 000	$48^2 \times 61$	0.23		Intermittent
80 000	$48^2 \times 61$	0.25	6(*c–f*)	Intermittent
85 000	$32^2 \times 41$	0.25		Intermittent
90 000	$48^2 \times 61$	0.28		Intermittent
100 000	$48^2 \times 61$	0.30	7(*a*, *b*)	Large-scale plumes

TABLE 3. Nonlinear runs: $\zeta = 1.2$, $Q = 1\,000$, $\lambda = 2$.

5.2. *From hexagons to chaos via intermittent bursts* ($\lambda = 2$)

Next we describe results for convection in a box with $\lambda = 2$, so that the area is doubled and patterns are less constrained by the finite aspect ratio. In the weakly nonlinear regime we might expect to find steady solutions with small transverse rolls or tiny squares and $k = 2\pi$.

The nonlinear results are summarized in table 3. For $R = 30\,000$ we find a steady solution – but the preferred pattern is one of irregular (deformed) hexagons with four plumes in the box. At the upper boundary magnetic flux is swept out of the broad rising plumes and confined to a network that surrounds them, with the strongest fields at corners in this network. At the bottom there is a complementary pattern, with strong fields at the centres of the plumes, while the field within the layer has an intermediate structure (cf. Weiss *et al.* 1996, figure 3). In an infinite layer regular hexagons would no doubt be preferred but their occurrence is precluded by imposing a square lattice (Matthews 1998): to obtain a regular pattern one should use a rectangular box with sides in the ratio $\sqrt{3}$:1 (cf. Paper I). In a stratified layer with strong fields, hexagons appear at a transcritical bifurcation and stable up-hexagons, with isolated rising plumes surrounded by a network of sinking material, exist below the bifurcation point. Matthews (1998) presents the weakly nonlinear theory both for the four-plume pattern (with D_{4h} spatial symmetry) and for the six-plume pattern found with $Q = 2\,000$ and $R = 100\,000$ (Weiss *et al.* 1996); a more complete treatment would have to include resonant interactions with modes generated by the rotational symmetry ρ of the square lattice (cf. Dionne, Silber & Skeldon 1997).

Steady solutions with irregular hexagons persist for $30\,000 \leqslant R \leqslant 65\,000$. Figures 6(*a*) and 6(*b*) show the patterns for $R = 40\,000$ and $R = 60\,000$, respectively. In each case the plumes appear in rows parallel to the x-axis. The plumes in each row have a separation $\lambda/2$ and their positions shift by $\lambda/4$ from one row to the next. The basic cell is a rectangle with sides in the ratio 1:2, elongated parallel to the y-axis, and there is obviously an equivalent solution obtained by rotating the whole pattern through 90°. The pattern in figure 6(*a*) has mirror symmetry about planes through each plume together with the translational symmetry $\tilde{\tau} : (x, y) \to (x + \lambda/4, y + \lambda/2)$ so the full spatial symmetry group is D_{4h}:

$$\{E, m_x, m_y, i, \tilde{\tau}, \tilde{\tau}m_x, \tilde{\tau}m_y, \tilde{\tau}i, \tilde{\tau}^2, \tilde{\tau}^2 m_x, \tilde{\tau}^2 m_y, \tilde{\tau}^2 i, \tilde{\tau}^3, \tilde{\tau}^3 m_x, \tilde{\tau}^3 m_y, \tilde{\tau}^3 i\}, \tag{5.1}$$

the product of D_4 (generated by m_x and $\tilde{\tau}$) and Z_2 (generated by m_y). When $R = 60\,000$, random perturbations develop into a transient solution that retains approximate D_{4h} symmetry but plumes in alternate rows rapidly develop different shapes. In figure 6(*b*),

https://doi.org/10.1017/S0022112000001373 Published online by Cambridge University Press

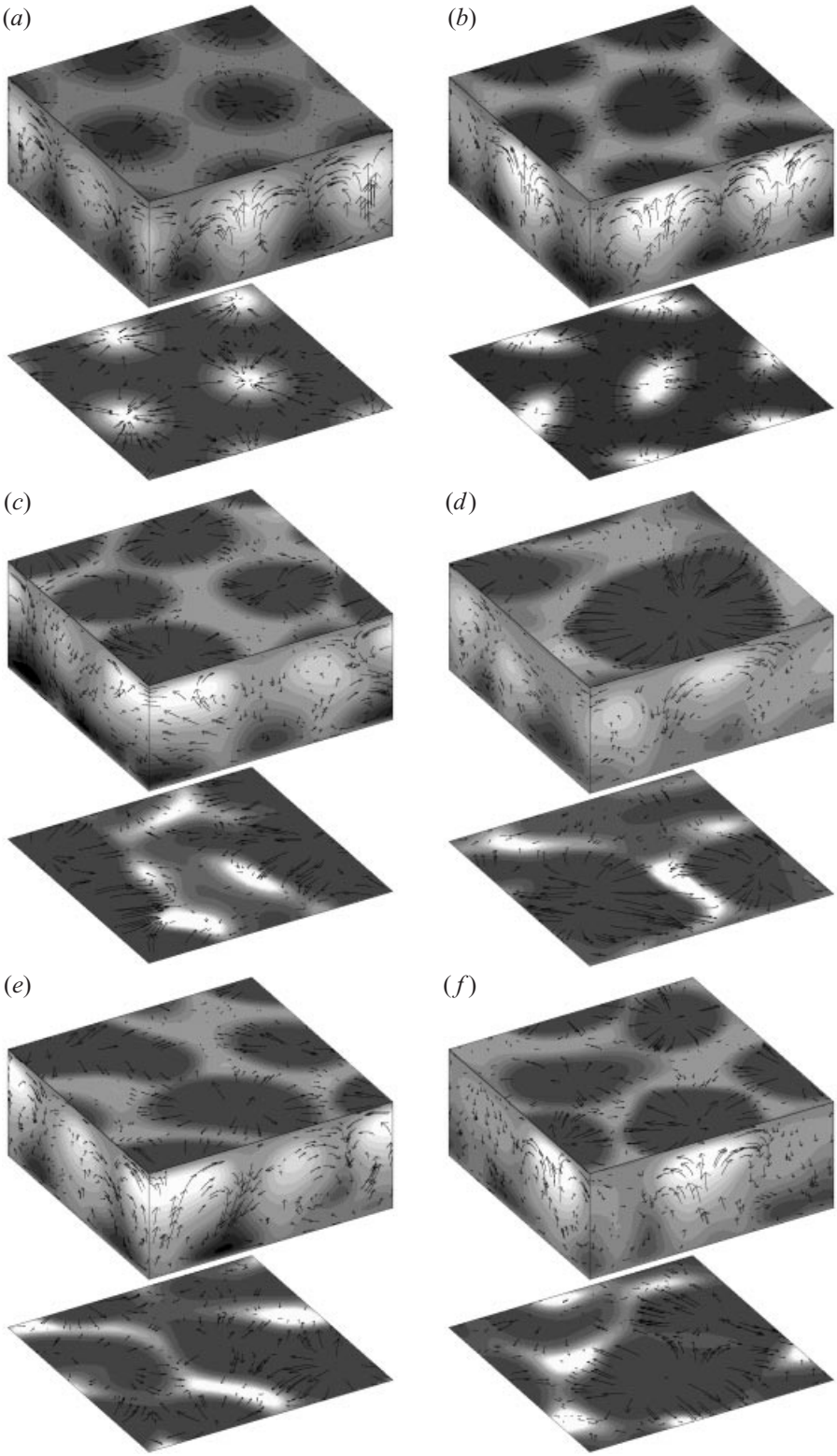


FIGURE 6. For caption see facing page.

https://doi.org/10.1017/S0022112000001373 Published online by Cambridge University Press

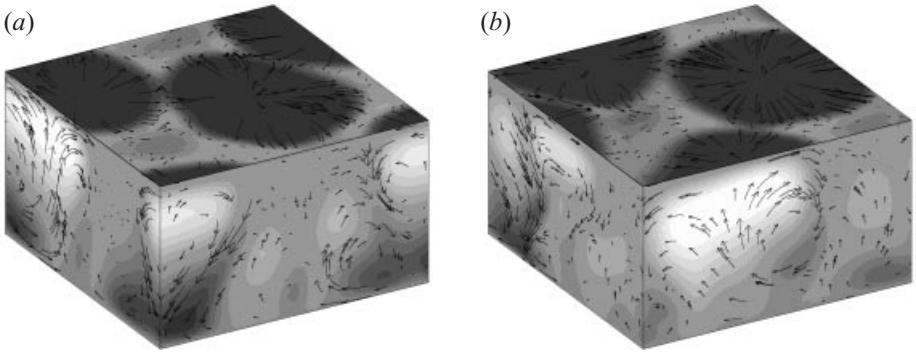


FIGURE 7. Large plumes for $\zeta = 1.2$, $Q = 1\,000$, $\lambda = 2$ and $R = 100\,000$. This pair of images shows time-dependent behaviour with an evolving magnetic network at the upper boundary.

which shows the final state, the plumes in alternate rows are elongated in different directions and so the pattern only has the symmetry group

$$\{E, i, \tilde{\tau}m_x, \tilde{\tau}m_y, \tilde{\tau}^2, \tilde{\tau}^2 i, \tilde{\tau}^3 m_x, \tilde{\tau}^3 m_y\} = D_4. \tag{5.2}$$

Apparently the translational symmetry $\tilde{\tau}$ is broken in a bifurcation at $R \approx 50\,000$. It can easily be verified that the appropriate representation of D_{4h} is one-dimensional and hence that this bifurcation must be a simple pitchfork.

With $R = 70\,000$ the D_4-symmetric pattern persists up to $t \approx 100$ but this behaviour proves to be intermittent. Almost symmetric patterns alternate aperiodically with episodes when plumes migrate and amalgamate, squeezing out their intermediate neighbours. Then a more or less symmetric four-plume pattern is restored, although the plumes are displaced from their original positions and the rows may be rotated through 90°. As R is increased these bursts become more violent. Figure 6(c–f) shows four stages during a typical episode with $R = 80\,000$: at first there are four irregular plumes but they evolve into a single dominant plume that almost fills the box; this plume then decays until the four-plume pattern reappears. When $R = 100\,000$ behaviour is chaotic, with one or two large plumes that confine magnetic flux to narrow lanes at the top of the layer; this solution is illustrated in figure 7 and it has already been discussed by Weiss *et al.* (1996 – see figure 2).

Physically, there is a transition from the tightly constrained pattern of small plumes on an almost hexagonal lattice that prevails when the magnetic field is dominant ($28\,000 \leqslant R \leqslant 65\,000$) to one of large chaotic plumes, when motion is dominated by buoyancy and the Lorentz force only matters locally in regions with strong fields ($R \geqslant 100\,000$). This transition is associated with a sequence of bifurcations in which symmetries are successively broken, and solutions becomes time-dependent and chaotic. We have not attempted to follow this bifurcation sequence but the intermediate regime ($70\,000 \leqslant R \leqslant 90\,000$) exhibits interesting features. Within the phase space of the system there is a pair of invariant subspaces with D_4 symmetry, corresponding to the two orientations of the rows of plumes, and each of these subspaces is itself the intersection of invariant subspaces. For a given value of R the unstable D_4-symmetric solutions lie on a pair of invariant two-tori within the

FIGURE 6. Three-dimensional solutions for $\zeta = 1.2$, $Q = 1\,000$, $\lambda = 2$: (a) irregular hexagons with D_{4h} symmetry ($R = 40\,000$); (b) asymmetric irregular hexagons with D_4 symmetry ($R = 60\,000$); (c–f) intermittent bursts ($R = 80\,000$).

https://doi.org/10.1017/S0022112000001373 Published online by Cambridge University Press

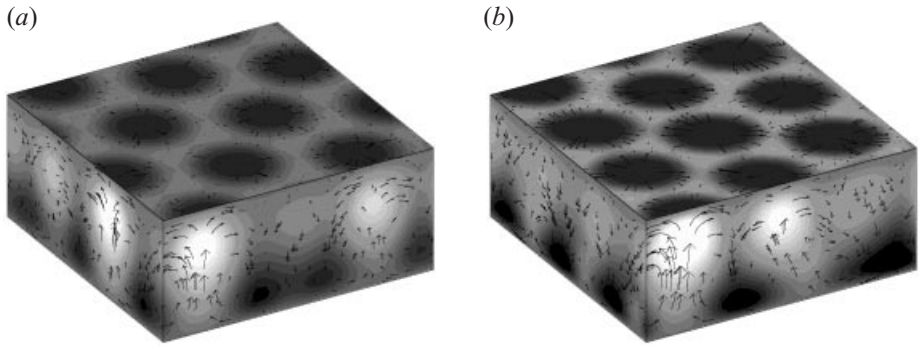


FIGURE 8. Irregular hexagons in a wider box: three-dimensional solutions for $\zeta = 1.2$, $Q = 1\,000$, $\lambda = \frac{8}{3}$ and $R = 45\,000$: (*a*) 8 plumes; (*b*) 9 plumes.

R	Mesh	$\langle u^2\rangle^{1/2}$	Figure	Type of solution
45 000	$32^2 \times 41$	0.12	8(*a*)	Irregular hexagons (8 plumes)
45 000	$32^2 \times 41$	0.12	8(*b*)	Irregular hexagons (9 plumes)
65 000	$32^2 \times 41$	0.17		Irregular hexagons (8 plumes)
65 000	$32^2 \times 41$	0.18		Time-dependent irregular hexagons (9 plumes)
70 000	$32^2 \times 41$	0.19		Irregular hexagons (8 plumes)
80 000	$32^2 \times 41$	0.23		Irregular hexagons, marginally stable (8 plumes)
90 000	$32^2 \times 41$	0.28		Intermittent
100 000	$48^2 \times 49$	0.32		Large plumes

TABLE 4. Nonlinear runs: $\zeta = 1.2$, $Q = 1\,000$, $\lambda = \frac{8}{3}$.

appropriate subspaces (since the plumes can be shifted in either direction) and there are further tori in the other invariant subspaces. The observed intermittency is associated with trajectories that linger in the neighbourhood of one or other of these invariant sets and then make a brief excursion away from them before returning either to the same neighbourhood or to that of another symmetric subspace. In this problem there is a chaotic attractor for large R (when there are only one or two plumes in the box). As R is progressively decreased this attractor approaches two or more invariant sets, and trajectories spend longer and longer in their neighbourhoods, until a pair of these sets eventually becomes attracting.

This bursting appears to be a form of on-off or in-out intermittency (Platt, Spiegel & Tresser 1993; Ashwin, Covas & Tavakol 1999). Such behaviour is often associated with the presence of symmetry-invariant subspaces and structurally stable heteroclinic orbits; studies of shearing instabilities in two- and three-dimensional convection or magnetoconvection provide specific examples of such orbits (Rucklidge & Matthews 1996; Matthews *et al.* 1996). There may also be chaotic attractors within the invariant subspaces, leading to blow-out bifurcations and cycling chaos (cf. Ashwin & Rucklidge 1998).

5.3. *Relaxing the geometrical constraint* $\left(\lambda = \frac{8}{3}\right)$

We next explore the effects of doubling the area of the box again so that it can contain twice as many plumes. Instead of setting the aspect ratio $\lambda = 2$ we therefore take $\lambda = 8/3$, corresponding to an increase in area by a factor 16/9. We have repeated the sequence of runs in order to test whether the approximately hexagonal pattern

https://doi.org/10.1017/S0022112000001373 Published online by Cambridge University Press

is preserved. The results are summarized in table 4. In the weakly nonlinear regime there are steady solutions with eight plumes lying on diagonal bands. At $R = 45\,000$ the system initially settles towards a pattern of very small squares ($k = 2.12\pi$) but this proves to be unstable (unlike the pattern found for $\lambda = 4/3$). The plumes on adjacent rows shift relative to each other to produce the irregular hexagonal pattern in figure 8(*a*). Matthews (1998) provides a description of the associated theory. The basic cell is a diagonally oriented rectangle with sides in the ratio 1:2. This solution, which is essentially the same as that in figure 6(*a*) but rotated through 45°, is stable for $45\,000 \leqslant R \leqslant 80\,000$; at $R = 45\,000$, however, we also find a stable solution with nine plumes in the box, which is shown in figure 8(*b*). They are again disposed on an irregular hexagonal lattice but the number of plumes is different and there is no reflection symmetry. Either of these solutions can appear in a subcritical secondary bifurcation from rolls and they have been discussed by Matthews (1998). In a large box we should expect that two or more irregular hexagonal patterns could be stable over a finite range of R. The nine-plume solution is delicate and has already become time-dependent at $R = 65\,000$ but the eight-plume hexagons persist to higher values of R than the four-plume patterns in § 5.2. These preferences are clearly sensitive to the precise value chosen for λ. At $R = 80\,000$ there are still irregular hexagons with eight plumes in the box but the plumes are markedly elongated in the direction of their nearest neighbours, imparting a linear structure without breaking any symmetry. This pattern, which resembles the 'hexarolls' described by Auer, Busse & Clever (1995), becomes unstable by $R = 90\,000$, when behaviour is intermittent with bursts when plumes amalgamate and convection is aperiodic. Finally, for $R = 100\,000$, the large-scale plumes take over, giving a pattern similar to that found in a smaller box (see Weiss *et al.* 1996).

These results confirm that the transitions found in § 5.2 are robust. The basic sequence, starting with steady convection in an irregular hexagonal pattern and proceeding via intermittent behaviour to chaotic large-scale plumes, is repeated. The wider boxes also allow a greater variety of patterns and so there are more invariant tori to be visited by trajectories in the intermittent regime – but these are only minor complications.

5.4. *Flux separation in very wide boxes* ($\lambda = 4, 8$)

We have gone on to investigate behaviour in even wider boxes, and the results are listed in table 5. With $\lambda = 4$, thereby doubling the area again, there are yet more plumes in the box and the constraints imposed by the square lattice are further relaxed, as shown for $R = 70\,000$ in figures 9(*a*) and 9(*b*). The overall pattern of intermittency is unchanged but bursting now occurs sporadically over the computational region, while smaller plumes return locally, without the symmetry associated with an invariant subspace. At $R = 100\,000$, the large-scale plumes congregate into clusters from which magnetic fields are excluded, leaving a broad magnetic network containing smaller, weaker structures (Tao *et al.* 1998). This pattern of incipient flux separation is displayed in figures 9(*c*) and 9(*d*).

The effects of a finite aspect ratio become much less significant for $\lambda \geqslant 8$. Figure 10 provides snapshots of a solution with $R = 100\,000$ and $\lambda = 8$. The box is now wide enough to allow long-wavelength modulation of the broad plumes in figure 7. In a run started from weak random perturbations to the static state, small plumes initially appear on a scale corresponding to the most unstable linear modes. These structures amalgamate into broad plumes and groups of these large plumes gradually cluster together, expelling magnetic flux into regions where the field is locally strong enough

https://doi.org/10.1017/S0022112000001373 Published online by Cambridge University Press

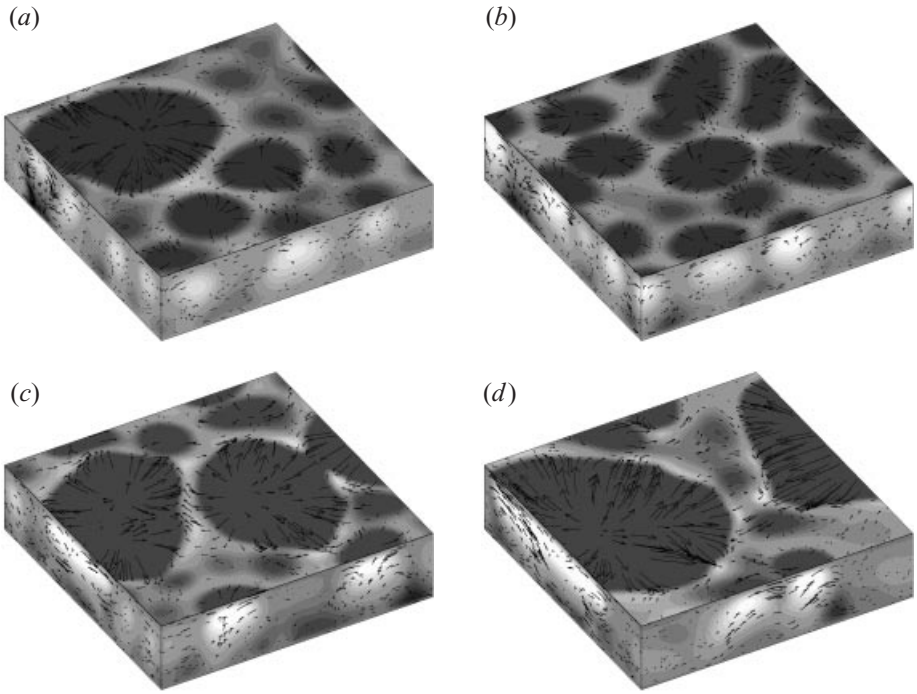


FIGURE 9. Bursting and large plumes in a wide box ($\lambda = 4$): three-dimensional solutions for $\zeta = 1.2$, $Q = 1\,000$. (a, b) Intermittent bursts ($R = 70\,000$); (c, d) large plumes ($R = 100\,000$), showing incipient flux separation.

λ	R	Mesh	$\langle u^2 \rangle^{1/2}$	Figure	Type of solution
4	70 000	$64^2 \times 41$	0.25	$9(a, b)$	Intermittent
4	80 000	$64^2 \times 41$	0.31		Intermittent
4	100 000	$128^2 \times 64$	0.36	$9(c, d)$	Large plumes
8	100 000	$256^2 \times 64$	0.36	$10(a, b)$	Large plumes, flux separation

TABLE 5. Nonlinear runs: $\zeta = 1.2$, $Q = 1\,000$, $\lambda = 4, 8$.

to impede convection. This new process of flux separation leads to a state where the motion and the magnetic field are segregated from each other (Tao *et al.* 1998). In regions where the field is strong, motion is restricted to slender and relatively feeble plumes, while regions with vigorous convection are almost field-free. The difference between values of B^2 in these regions is apparent in figure 10(a), while figure 10(b) demonstrates that there are clusters of plumes in the 'field-free' regions.

In the patches where the field is weak patterns should be similar, locally, to those for convection with $R = 100\,000$ and $Q \ll 1\,000$. Hence we expect to find a more vigorous version of the plumes in figure 3. The time-dependent results show that plumes within the clusters are continually splitting and evolving (Tao *et al.* 1998), as in various other simulations of compressible convection in the absence of a magnetic field (e.g. Cattaneo *et al.* 1991; Stein & Nordlund 1998). Where the field is strong we expect to see local patterns that are similar to those that would be obtained with $R = 100\,000$ and, say, $Q \approx 2\,000$. The plumes are small and ineffective

https://doi.org/10.1017/S0022112000001373 Published online by Cambridge University Press

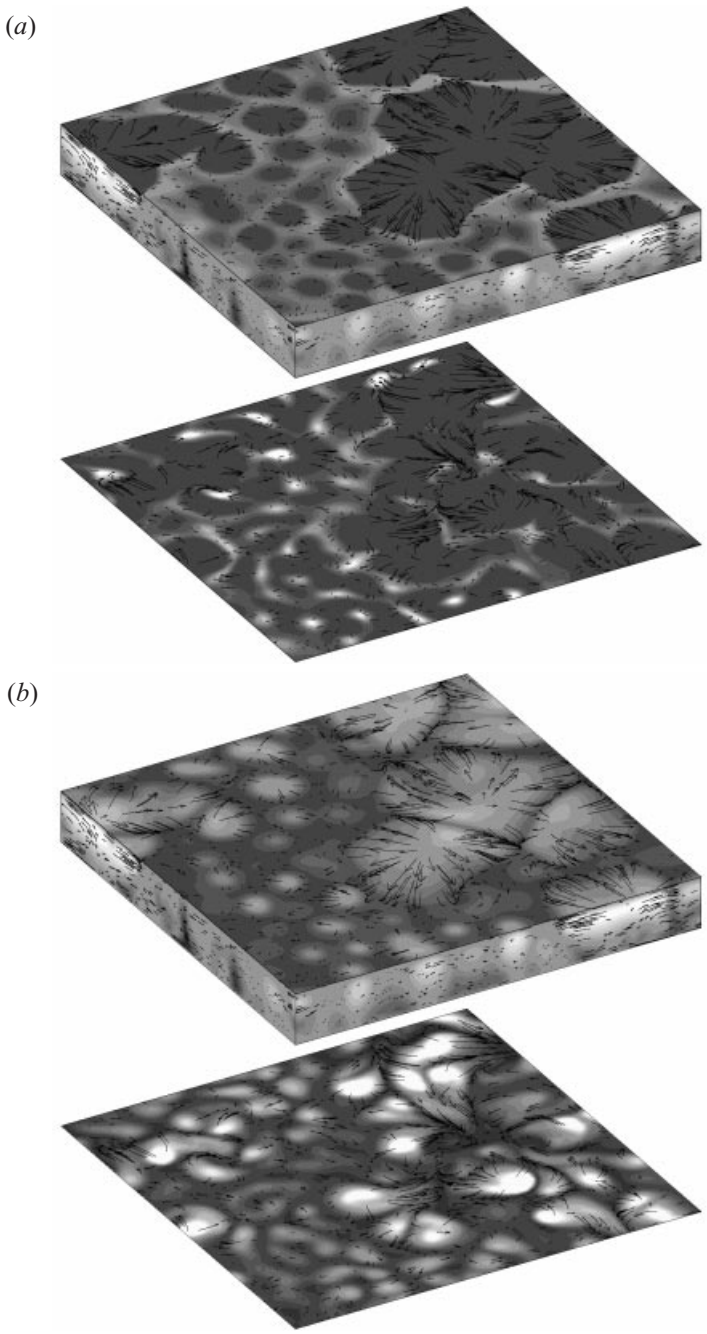


FIGURE 10. Flux separation in a very wide box ($\lambda = 8$): snapshots of a three-dimensional solution for $\zeta = 1.2$, $Q = 1\,000$ and $R = 100\,000$, showing (*a*) the square of the magnetic field strength, and (*b*) the vertical temperature gradient on the upper and lower boundaries. The broad and vigorous plumes assemble into clusters and succeed in expelling magnetic flux into a region where the field is locally so strong that only small-scale convection can occur. The cool sinking plumes impinging on the lower boundary show that the field-free regions have a complicated structure.

https://doi.org/10.1017/S0022112000001373 Published online by Cambridge University Press

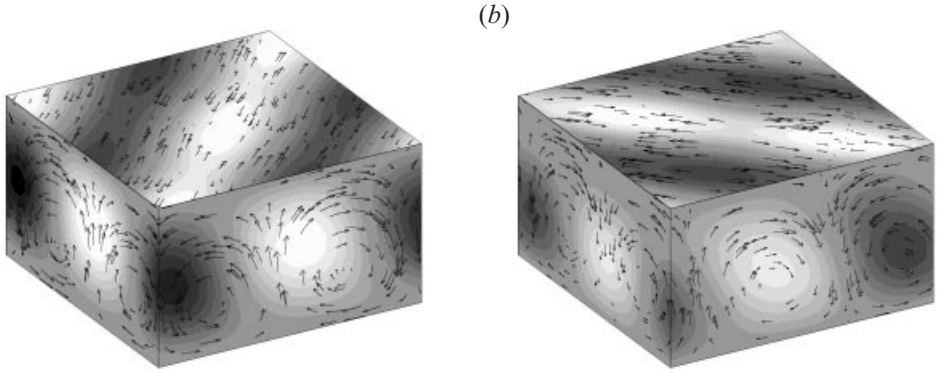


FIGURE 11. Three-dimensional oscillatory solutions for $\zeta = 0.6$, $Q = 2\,000$, $\lambda = 2$ and $R = 30\,000$. Diagonal alternating rolls for (*a*) $t = 1409.2$, (*b*) $t = 1410.9$.

at transporting heat, as is apparent from figure 10(*b*). At any instant the spatial pattern is irregular and video sequences show that individual plumes grow, decay and disappear aperiodically. This pattern of spatiotemporal disorder can be related to the ordered but aperiodic oscillations found, for instance, in a run with $R = 100\,000$ and $Q = 1\,400$ when activity is constrained by setting $\lambda = 2$ (Weiss *et al.* 1996 – see figure 1*c*). In that case the basic hexagonal pattern persists but undergoes spatially modulated oscillations which are a three-dimensional version of the two-dimensional oscillations found for $\lambda = \frac{4}{3}$ and exhibited in figure 4(*c*, *d*). When the aspect ratio is increased these oscillations become wilder and increasingly disordered. Nevertheless, the periodic modulation found first in two-dimensional runs (Weiss *et al.* 1990) and then in narrow boxes serves as a guide to interpreting the behaviour seen in patches where the fields are strong in figure 10.

6. Oscillatory convection ($\zeta = 0.6$)

When the diffusivity ratio is less than unity over most of the layer, convection sets in at an oscillatory bifurcation for Q sufficiently large. Then there are five possible stable patterns on a square lattice (Silber & Knobloch 1991; Clune & Knobloch 1994; Paper I). These include travelling rolls and travelling squares, with $O(2)$ and Z_2 spatial symmetry, respectively; standing rolls and standing squares, with $Z_2 \otimes O(2)$ and D_4 spatial symmetry, respectively; and alternating rolls, with D_2 symmetry. These solutions also possess additional spatiotemporal symmetries. Both in the Boussinesq regime (Clune & Knobloch 1994) and in a shallow stratified layer (Paper I) there is a wide parameter range over which both travelling and alternating rolls are stable. With $\zeta = 0.6$ and $Q = 2\,000$ the Hopf bifurcation first occurs for $R_c^{(o)} = 29\,800$ and $k_c = 1.50\pi$.

In a square box with $\lambda = 2$ we therefore expect to find time-dependent diagonal alternating rolls and small squares, with $k = \sqrt{2}\pi$, near the initial bifurcation. Table 6 lists the nonlinear results. There is a hint of subcritical behaviour leading to diagonal travelling rolls for $R < R^{(o)}$ but by $R = 30\,000$ the rolls are replaced by small standing squares, which develop on an extremely long timescale into diagonal alternating rolls. This pattern is displayed in figures 11(*a*) and 11(*b*). By $R = 37\,000$ the diagonal rolls are supplanted by weakly modulated transverse alternating rolls which in turn give way to large standing squares that are asymmetric and irregularly modulated. When $R = 40\,000$ the pattern shifts erratically from one oscillatory state to another: intervals

https://doi.org/10.1017/S0022112000001373 Published online by Cambridge University Press

R	Mesh	$\langle u^2\rangle^{1/2}$	Figure	Type of solution
30 000	$32^2 \times 41$	0.027	11(a, b)	Diagonal alternating rolls
37 000	$32^2 \times 41$	0.055		Modulated standing squares
40 000	$32^2 \times 41$	0.060		Intermittent
50 000	$48^2 \times 61$	0.11		Large plumes

TABLE 6. Nonlinear runs: $\zeta = 0.6$, $Q = 2\,000$, $\lambda = 2$.

of regularity with asymmetric alternating rolls or standing squares are interrupted by bursts of disordered behaviour. Finally, when $R = 50\,000$ the system settles down to a pattern that is wildly irregular in both space and time, with motion dominated by broad rising plumes; magnetic flux is confined to a network at the top and to isolated flux tubes at the base.

With a lower magnetic diffusivity the field is more closely tied to the fluid and behaviour is dynamically more active. We have not attempted to establish the relative stability of different oscillatory patterns in the weakly nonlinear regime. What the solutions show is again a transition from magnetically dominated behaviour – which is now oscillatory – to a regime where the magnetic structure accommodates itself to the pattern of large-scale convective plumes. As in § 5, the intermediate regime exhibits intermittent bursts. However, a greater variety of behaviour is now possible. Not only may the patterns change in scale and orientation but the chaotic trajectory may also approach any of the oscillatory solutions. So an interval with alternating rolls may be followed by one with standing squares, and there is scope for chaotic behaviour within any of the invariant subspaces.

7. Patterns forced by a square lattice ($\zeta = 6$)

In this section we investigate nonlinear convection with $Q = 200$ and $\zeta = 6$; thus the diffusivity ratio increases from unity at the top of the layer to 11 at the bottom, and the initial bifurcation leads to steady convection. From figure 1, convection sets in with a wavenumber $k \approx 1.5\pi$, which is significantly greater than that for $\zeta = 1.2$ in § 5. Thus solutions are more sensitive to the choice of aspect ratio.

7.1. *Rolls, squares, waves and wobblers* ($\lambda = 2$)

Following the treatments in the previous two sections, we start by considering a box with aspect ratio $\lambda = 2$, where we expect to find either small squares or diagonal rolls, with $k = \sqrt{2}\pi$. Table 7 summarizes the results of these numerical experiments, which reveal a fascinating sequence of transitions. We first describe the computational results and then discuss the symmetries of the numerical solutions in order to establish the underlying bifurcation structure. In this process the strength of the group-theoretic approach is clearly demonstrated.

For $R = 10\,000$, just above the onset of convection, a random perturbation develops rapidly into an apparently steady pattern of small squares, with D_{4h} symmetry. The squares survive up to $t = 100$ but then gradually give way to diagonal rolls for $t > 200$. The final state, shown in figure 2(d), has approximate $D_2 \otimes O(2)$ symmetry. Close inspection of the solution actually reveals slight deviations from $O(2)$ symmetry that persist at least up to $t = 500$, indicating that varicose rolls are the only stable pattern for this value of R. This is an example of a symmetry-breaking bifurcation, as

https://doi.org/10.1017/S0022112000001373 Published online by Cambridge University Press

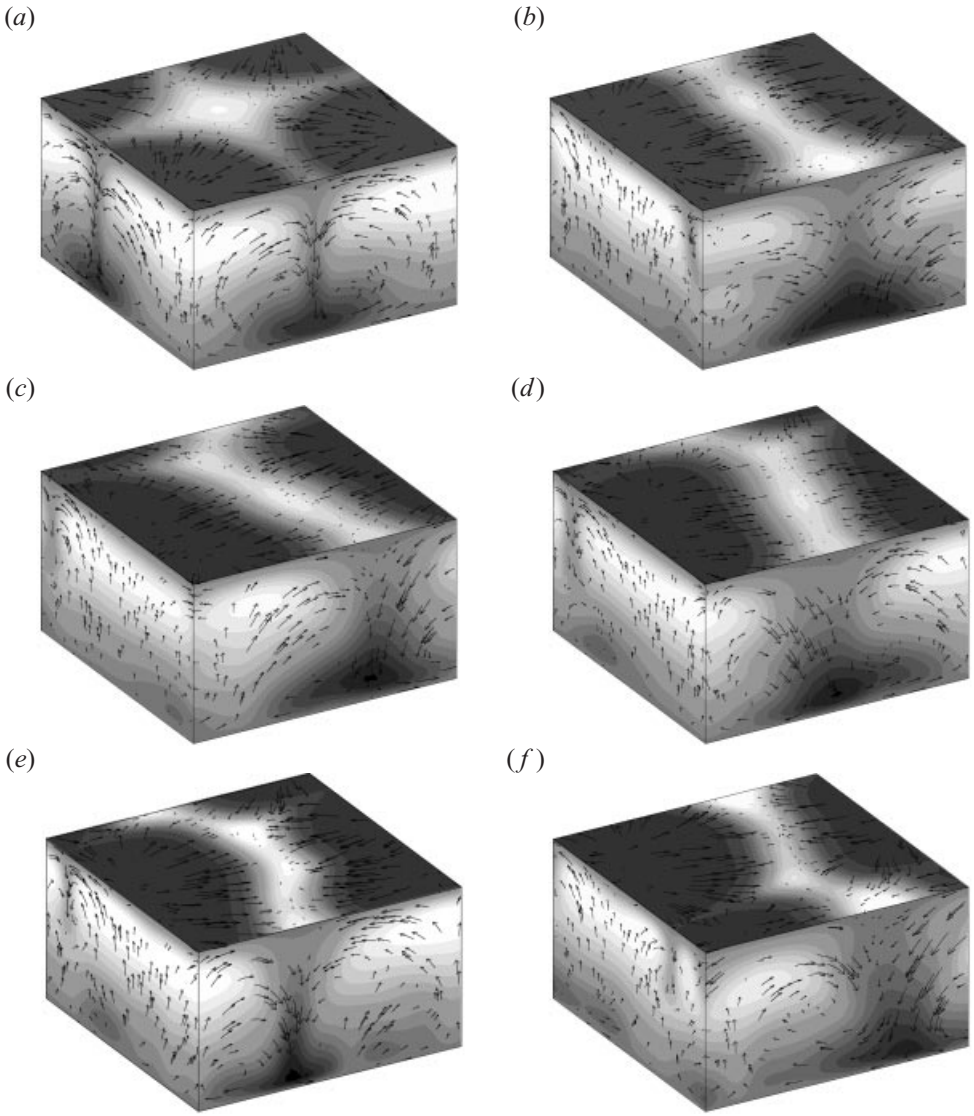


FIGURE 12. Three-dimensional solutions for $\zeta = 6$, $Q = 200$: (*a*) Large squares and (*b*) travelling waves (both for $R = 60\,000$); (*c*,*d*) wobblers for $R = 55\,000$ ($t = 130$, 140); (*e*,*f*) chaotically modulated TW for $R = 100\,000$ ($t = 134$, 159).

mentioned above in § 3.1; a similar transition was described in Paper I. By $R = 20\,000$ the small squares are stable and the resulting pattern is displayed in figure 2(*b*). When that solution is used to provide initial conditions for a run at $R = 30\,000$ the two plumes merge and the small squares develop into large squares, with a single plume in the box (cf. Proctor & Matthews 1996): the solution displayed in figure 2(*a*) has D_4 symmetry. By using solutions obtained at lower values of R as initial conditions it is possible to obtain stable large-square patterns up to $R = 65\,000$. In figure 12(*a*) we illustrate the solution for $R = 60\,000$. When $R = 70\,000$ the squares become unstable and develop into travelling waves.

Figure 12(*b*) shows a solution for the same value of R as that in figure 12(*a*)

https://doi.org/10.1017/S0022112000001373 Published online by Cambridge University Press

R	Mesh	$\langle u^2\rangle^{1/2}$	Figure	Type of solution
10 000	$32^2 \times 41$	0.09	2(*d*)	Varicose diagonal rolls
20 000	$32^2 \times 41$	0.21	2(*b*)	Small squares
30 000	$32^2 \times 41$	0.23	2(*a*)	Large squares (from $R = 20\,000$)
30 000	$32^2 \times 41$	0.23		Large squares (from wobblers at $R = 50\,000$)
40 000	$32^2 \times 41$	0.28		Large squares (from $R = 30\,000$)
40 000	$32^2 \times 41$	0.28		Weakly wobbling (from wobblers at $R = 50\,000$)
50 000	$32^2 \times 41$	0.28		Large squares (from $R = 40\,000$)
50 000	$32^2 \times 41$	0.28		Wobblers (from scratch)
55 000	$32^2 \times 41$	0.30	12(*c*, *d*)	Wobblers (from scratch)
60 000	$48^2 \times 61$	0.34	12(*a*)	Large squares (from $R = 40\,000$)
60 000	$48^2 \times 61$	0.32	12(*b*)	Travelling waves (from scratch)
65 000	$48^2 \times 61$	0.35		Large squares (from $R = 60\,000$)
65 000	$32^2 \times 41$	0.32		Travelling waves (from $R = 60\,000$)
70 000	$48^2 \times 61$	0.34		Weakly modulated travelling waves (from scratch)
70 000	$48^2 \times 61$	0.34		Weakly modulated travelling waves (from squares)
80 000	$48^2 \times 61$	0.34		Aperiodically modulated travelling waves (from scratch)
100 000	$48^2 \times 61$	0.38	12(*e*, *f*)	Wildly modulated travelling waves (from scratch)

TABLE 7. Nonlinear runs: $\zeta = 6$, $Q = 200$, $\lambda = 2$.

but started this time from a random perturbation to the static reference state. The attracting solution is a travelling wave (with a weak decaying modulation). Adjacent plumes have merged to give a structure that is elongated in the direction of propagation, with strong magnetic fields in an irregular strip between the rising plumes at the top, and beneath them at the base. Decreasing R leads to periodic oscillations that are stationary in space. Figures 12(*c*) and 12(*d*) show opposite phases of the time-dependent solution at $R = 55\,000$. The rising plumes swing to and fro and the upper flux concentration moves between them. We shall refer to these standing wave solutions as 'wobblers', to distinguish them from the 'breathers' discussed e.g. by Hirschberg & Knobloch (1993). Wobblers persist as R is further reduced down to $R = 40\,000$ though the periodic variations decrease in amplitude. When $R = 30\,000$ a run started from a wobbler at higher R develops into steady squares.

When $R \geqslant 70\,000$ the travelling waves are modulated. Over the range $80\,000 \leqslant R \leqslant 100\,000$ the modulation is chaotic, growing wilder and more erratic with increasing R. In figures 12(*e*) and 12(*f*) we show two different states for $R = 100\,000$: the pattern still drifts but changes aperiodically as it moves. From a physical point of view there is a competition between the Lorentz force, which favours travelling waves, and the effects of buoyancy, which lead to broad upwelling plumes. If R were yet further increased the latter would eventually predominate and the pattern would come to resemble that in figure 3.

The challenge now is to assemble these transitions into a sensible and coherent structure. Planform changes in the mildly nonlinear regime ($R^{(e)} < R \leqslant 30\,000$) are comparatively straightforward and the corresponding bifurcation structure is shown schematically in figure 13(*a*). Behaviour near the onset of convection is described by the normal form equations (A 6), where a_1, a_2 now represent the amplitudes of diagonal rolls with symmetries m_d, $m_{d'}$, respectively; the $(a, 0)$ and $(0, a)$ fixed points correspond to steady diagonal rolls, while the $(a, \pm a)$ solutions represent small squares. The latter do not show the strong up–down asymmetry that appeared at low β in a

https://doi.org/10.1017/S0022112000001373 Published online by Cambridge University Press

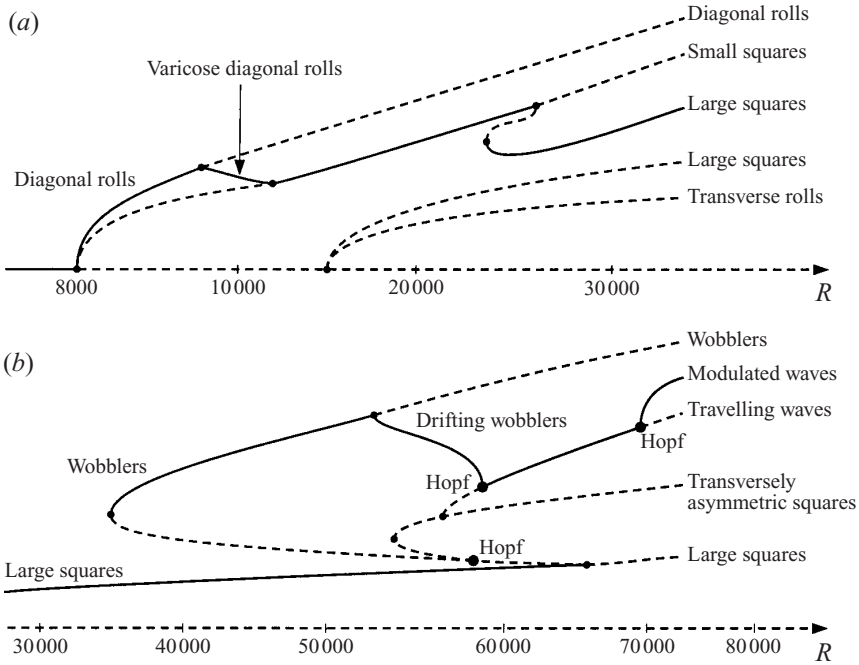


FIGURE 13. Schematic bifurcation diagrams for $\zeta = 6$, $Q = 200$, $\lambda = 2$: (*a*) the mildly nonlinear regime, showing transitions from rolls to squares; (*b*) the fully nonlinear regime, showing the origin of the wobblers.

shallow layer (see Paper I). The solution branches apparently bifurcate supercritically and rolls are initially preferred; a secondary symmetry-breaking bifurcation (also supercritical) leads to a mixed-mode branch of asymmetric solutions with D_2 symmetry (cf. figure 2*d*) and stability is transferred to small squares. As R is further increased, together with β, modes with smaller wavenumbers bifurcate from the trivial solution. The first to appear are transverse rolls and large squares, with $k = \pi$. They are initially unstable to perturbations with $k = \sqrt{2}\pi$ but stability is transferred from small squares to large squares by $R = 30\,000$; the transient behaviour suggests that this is an abrupt transition. Small squares possess the D_4 symmetry of (3.1) together with the translational symmetry $\tau : (x, y) \to (x + \lambda/2,\ y + \lambda/2)$, so their spatial symmetry group is D_{4h}. Breaking the symmetry τ in a pitchfork bifurcation gives rise to a pair of solution branches with the D_4 symmetry of large squares (cf. Proctor & Matthews 1996). Our results suggest that the pitchfork is subcritical and that the solutions acquire stability in a saddle-node bifurcation (with associated hysteresis), as indicated in figure 13(*a*), while the large-square branch that bifurcates from the trivial solution never gains stability. (It is not possible for the latter branch to acquire stability from small squares through an intermediate branch.)

Subsequent behaviour grows more complicated. Large squares remain stable up to $R \approx 65\,000$, when there is an abrupt transition to transverse travelling waves. This clearly requires a subcritical bifurcation. Although travelling waves can appear after a single bifurcation from stationary squares (as explained in § A.3) that does not readily account for the wobblers that exist for $40\,000 \leqslant R \leqslant 55\,000$. The solution illustrated in figures 12(*c*) and 12(*d*) possesses the point symmetry i together with the

https://doi.org/10.1017/S0022112000001373 Published online by Cambridge University Press

λ	R	Mesh	$\langle u^2\rangle^{1/2}$	Figure	Type of solution
8/3	20 000	$48^2 \times 41$	0.19		tiny rolls (slightly varicose)
8/3	30 000	$48^2 \times 41$	0.24	14(*a–d*)	intermittent squares
8/3	40 000	$48^2 \times 41$	0.28		intermittent squares
10/3	30 000	$48^2 \times 41$	0.24		intermittent squares
4	30 000	$64^2 \times 64$	0.25	14(*e*, *f*)	intermittent hexagons

TABLE 8. Nonlinear runs: $\zeta = 6$, $Q = 200$, $\lambda = \frac{8}{3}, \frac{10}{3}, 4$.

spatiotemporal symmetry t_y, corresponding to an advance of half a period in time plus reflection about a vertical plane parallel to the y-axis. The symmetry group of wobblers is therefore $\{E, i, t_x, t_y\} = D_2$ and so there are analogies between them and pulsating waves in two-dimensional Boussinesq magnetoconvection (Matthews *et al.* 1993; Rucklidge & Matthews 1996).

The existence of wobblers, with D_2 spatiotemporal symmetry, can only be explained by recourse to the arguments developed in the Appendix. As explained there, the wobblers cannot lie on a solution branch that bifurcates directly either from a branch of large squares (with D_4 spatial symmetry) or from one of travelling waves (with Z_2 spatial symmetry). The route from squares involves a symmetry-breaking pitchfork bifurcation to a steady pattern with the rectangular D_2 spatial symmetry as in figure 15(d'), followed by a Hopf bifurcation. That from travelling waves requires a Hopf bifurcation to modulated waves followed by a reverse pitchfork bifurcation. To determine what happens here we inspect the transient behaviour before and after the subcritical bifurcation from large squares. The run at $R = 30\,000$ that was started from a wobbler solution rapidly settled to a pattern with D_2 symmetry before eventually gaining the full D_4 symmetry of large squares. That implies that the most slowly decaying mode corresponds to a symmetry-breaking perturbation, and hence that there is a subcritical pitchfork bifurcation at $R \approx 67\,000$ to steady solutions with D_2 spatial symmetry. These undergo a Hopf bifurcation yielding a branch of wobblers, which gain stability in a saddle-node bifurcation around $R \approx 35\,000$, as sketched in figure 13(b). The remaining bifurcations in the figure are a saddle-node on the steady branch with D_2 spatial symmetry, followed by a supercritical pitchfork bifurcation to travelling waves with Z_2 spatial symmetry. The travelling waves eventually gain stability from the wobblers via an intermediate branch of modulated travelling waves (with t_x or t_y symmetry in a moving frame). This branch links a Hopf bifurcation from travelling waves to a pitchfork bifurcation from the wobblers. Then, as R is further increased, there is a final Hopf bifurcation at which the Z_2 symmetry of the travelling waves is broken, followed by a transition to chaotic modulation as magnetic effects become progressively less important.

The two bifurcation diagrams in figure 13 then summarize the disparate results of these numerical experiments. The transfer of stability from large squares to wobblers is made through an intermediate D_2-symmetric branch of transversely asymmetric squares, which never itself gains stability. Once again, these diagrams are minimal, though fortunately all representations at the bifurcation points are one-dimensional. It is abundantly clear from our discussion that it would not be possible to construct such a diagram without establishing the symmetries of the numerical solutions and then considering the constraints on transitions from one symmetry group to another.

https://doi.org/10.1017/S0022112000001373 Published online by Cambridge University Press

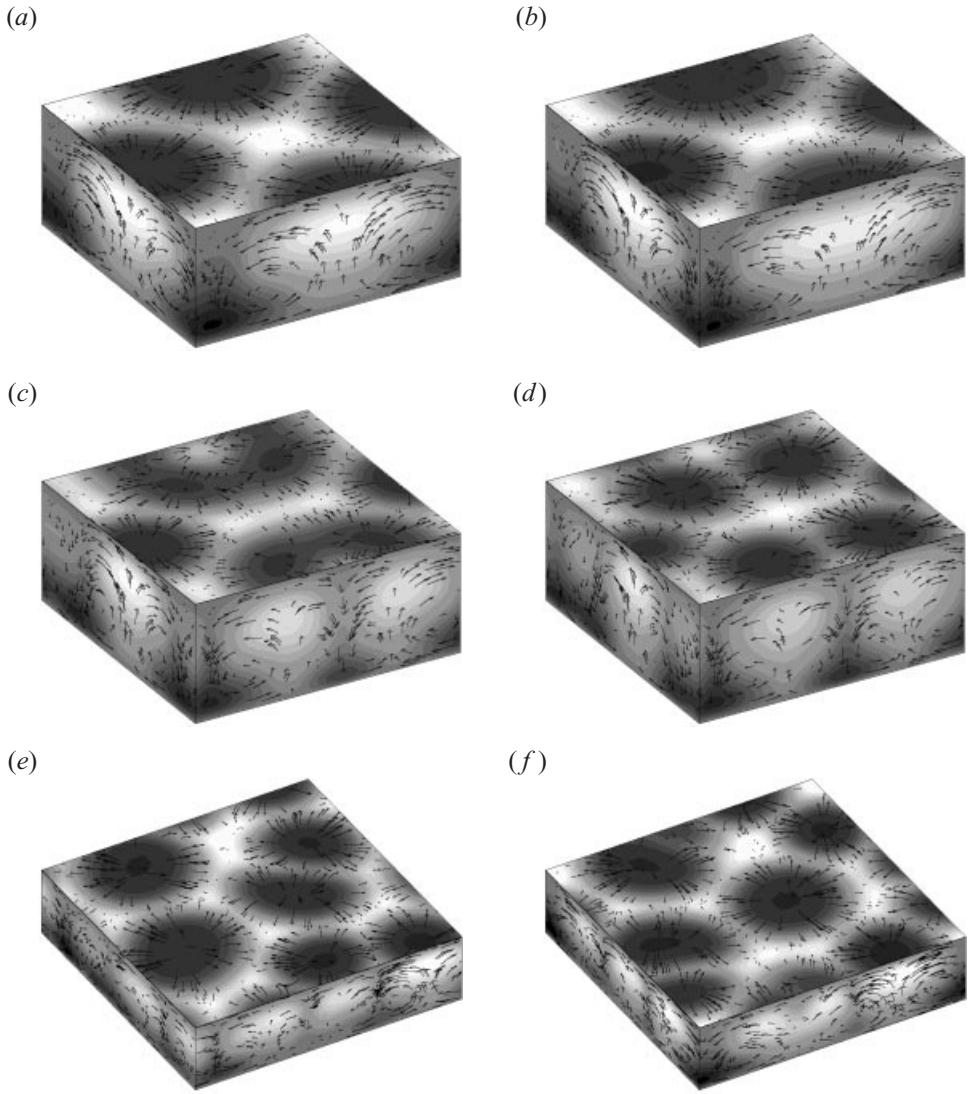


FIGURE 14. Increasing the aspect ratio: three-dimensional solutions for $\zeta = 6$, $Q = 200$, $R = 30\,000$. Time dependence for $\lambda = 8/3$: (*a*) small squares; (*b*) symmetry breaking; (*c*) fragmenting rings; (*d*) asymmetric tiny squares. (*e*, *f*) Chaotic hexagons for $\lambda = 4$.

7.2. *From squares to hexagons as the aspect ratio is increased* $\left(\lambda = \frac{8}{3},\ \frac{10}{3}, 4\right)$

We have also repeated some of the runs for $\zeta = 6$ and $Q = 200$ in wider boxes in order to discover whether the square patterns described in § 7.1 persist as λ is increased. These results are listed in table 8. With $\lambda = \frac{8}{3}$ we find for $R = 20\,000$ that small disturbances initially develop into a pattern of tiny squares with four plumes in the box and $k = 1.5\pi$ (virtually the same as the small squares with $k = \sqrt{2}\pi$ that are stable when $\lambda = 2$) – but eventually the squares give way to slightly varicose tiny rolls (similar to those found for $R = 10\,000$ when $\lambda = 2$). Apparently the bifurcation that breaks the $O(2)$ symmetry of rolls has been displaced to a higher value of R.

The effects of relaxing the constraints imposed by narrow boxes become more apparent as the Rayleigh number is increased. The steady squares found at $R = 30\,000$

https://doi.org/10.1017/S0022112000001373 Published online by Cambridge University Press

when $\lambda = 2$ (with $k = \pi$ and a single plume in the box) are replaced by time-dependent behaviour, illustrated in figure 14(*a–d*). Almost perfect small squares (with $k = 1.06\pi$ and two plumes in the box) are formed but they lose their translational symmetry and the square symmetry is then broken by a rectangular perturbation. Next, alternate plumes develop an annular structure with a sinking core and then split apart to form imperfect tiny squares (with five plumes). Thereafter the solution cycles aperiodically between these states. Similar, though less regular, behaviour persists with $R = 40\,000$.

Raising the aspect ratio to $\lambda = \frac{10}{3}$ allows more vigorous time-dependence for $R = 30\,000$ but there are still intermittent squares. However, the influence of the square lattice is markedly reduced when $\lambda = 4$ (a fourfold increase over the original area). Convection is strongly aperiodic but the plumes now tend to be disposed in patterns that are roughly hexagonal. Figures 14(*e*) and 14(*f*) show different arrangements, each with five plumes in the box. As time progresses, one or other of the plumes expands and splits, while one of its neighbours gets squeezed out of existence, so that the five-plume pattern is restored. This behaviour differs from that found with $\zeta = 1.2$, where plumes *merge* in the regime where bursts appear.

Comparing the four runs with $R = 30\,000$ we see that as the aspect ratio is increased steady convection gives way to time-dependent behaviour. The number of plumes in the box increases approximately in proportion to its area but steady square patterns become unstable to symmetry-breaking perturbations and are eventually replaced by roughly hexagonal arrays. Increasing R would no doubt lead to intermittent behaviour and the development of larger plumes. We do not, however, expect to see flux separation when $\eta > \kappa$ throughout the layer.

8. Discussion

In trying to extract generic patterns of behaviour from specific model calculations our principal concern has been to investigate transitions from order to disorder as a control parameter is increased. The results quoted, which are based on a total of over 90 separate runs, make it possible to contrast the various patterns that are found, and show how important it is to discover the effects of varying all the key parameters in a numerical investigation. As the Rayleigh number is raised the planform evolves from ordered states to ones with irregular arrangements of broad aperiodic plumes. These broad expanding plumes reappear whenever magnetic fields are dominated by the motion. In a system with symmetries the initial instability gives rise to several different planforms, one or other of which may be preferred in the weakly nonlinear regime. We have found both steady and periodic solutions, involving rolls, squares and hexagons. There is then a transition, involving a complex sequence of bifurcations, to spatiotemporal chaos and we have focused on pattern formation in this intermediate regime. The transition is typically associated with intermittent bursts, which may involve spatially modulated oscillations and merging or splitting of individual plumes. The behaviour found depends on the diffusivity ratio: for ζ sufficiently small we expect to see oscillations when the Lorentz force is dominant, and flux separation when convection is extremely vigorous.

The structures found in numerical experiments are obviously sensitive to the imposed lattice structure. It is convenient to choose a square box and then to vary the geometrical parameter λ. In the nonlinear regime the pattern adapts itself to the size of the box in order to attain an appropriate horizontal scale: an extreme example is the appearance of two-dimensional rolls in § 5.1. The square lattice also favours square planforms as opposed to hexagons. In general we expect to find stable hexagons near

https://doi.org/10.1017/S0022112000001373 Published online by Cambridge University Press

the onset of convection in a stratified layer, or whenever the up–down symmetry is broken (cf. Hoyle 1998). A deformed hexagonal pattern requires the presence of at least four plumes in the box (Matthews 1998), so a pattern of small squares (with two plumes) or large squares (with a single plume) may well be superseded by hexagons if λ is doubled or quadrupled, as happened in §§5.2 and 7.2. Furthermore, patterns that are steady in small boxes may become time-dependent when the aspect ratio is increased, as in §7.2. Fortunately the cell size is reduced when the magnetic field is dynamically important. With $\zeta = 1.2$ an aspect ratio $\lambda = 2$ is generally adequate in the weakly linear and intermediate regimes, though much larger boxes are needed in order to represent the long-wavelength modulation that leads to flux separation.

By classifying symmetries and detecting symmetry breaking, it is possible not only to describe planform changes but also to provide a model of the bifurcation structure even in comparatively complicated situations. Our results demonstrate the power and also the limitations of a group-theoretic approach. The most interesting bifurcation sequences appear when transitions are constrained by imposing a small aspect ratio, as in §§5.1 and 7.1, and the approach based on symmetries is most effective when there are only a few unstable modes. That is the case near the critical Rayleigh number for a small box, where the lattice imposes discrete wavenumbers that are sparsely spaced. For instance, the wavenumbers for small squares and large squares in §7.1 differ only by $\sqrt{2}$; no other wavenumbers are involved and many symmetries are shared. As the aspect ratio is increased, more and more unstable modes appear, together with the possibility of long-wavelength modulation. So the method fails as $\lambda \to \infty$, when the system becomes more nearly homogeneous and isotropic. Nevertheless, careful interpretation of results obtained in relatively small boxes can illuminate behaviour with much larger aspect ratios.

The general theory of symmetry-breaking transitions has been available for some time (e.g. Golubitsky *et al.* 1988; Rucklidge & Silber 1998) but is often couched in technical terminology. The theory is essential in explaining transitions that we have observed, and we attempt to present it accessibly in the Appendix. The simple groups (Z_2, D_2) can readily be dealt with directly; the same approach can also be applied to D_4, as in §A.1, though there are subtleties that are easy to overlook; but representations and equivariant bifurcation theory (§§A.2 and A.3) form the only option once more complicated groups are involved. Although we confine our attention here to patterns with square symmetry, the same approach can also be applied to hexagons.

Much of the original motivation for developing the theory of bifurcations with symmetry came from fluid mechanical experiments in the laboratory. Experimental observations of spatially periodic square patterns have been reported in many different systems, for both small and large boxes. The most obvious examples include Rayleigh–Bénard convection (Oliver & Booker 1983), binary fluid convection (Moses & Steinberg 1991), rotating convection (Bajaj *et al.* 1998), and Faraday surface wave experiments (Edwards & Fauve 1994). Hexagonal patterns are also widely observed. As the level of forcing is increased, these ordered patterns become unstable by a variety of mechanisms (Busse & Clever 1998); as well as instabilities that preserve some spatial periodicities there are others that involve long-wavelength modulations.

In many cases, the symmetry groups involved are straightforward. Interactions of modes with different symmetries in small square boxes, in which only a few modes are excited, allow close connections to be made between experiment and theory. A good example of this is Bénard–Marangoni convection, where the first convective pattern found by Ondarçuhu *et al.* (1993) had the full D_4 symmetry of the container and subse-

https://doi.org/10.1017/S0022112000001373 Published online by Cambridge University Press

quently lost stability to form a new state that was invariant under diagonal reflections. At higher Rayleigh number, the pattern oscillated periodically, acquiring a spatiotemporal symmetry that has been observed in large boxes too (Eckert, Bestehorn & Thess 1998). Another clear example involves sextupling of the spatial period of a pattern of hexagons in a large aspect ratio Faraday wave experiment (Kudrolli, Pier & Gollub 1998). The analysis of this transition requires a 288-element group (Tse *et al.* 2000).

Another feature of our numerical experiments is the appearance of intermittent bursts. These occur in many other situations (Knobloch & Moehlis 1999), often involving slow–fast dynamics, and are frequently associated with symmetry breaking and transitions between patterns with different scales (Moehlis & Knobloch 1998). Examples of bursting arise in binary convection (Sullivan & Ahlers 1988), as well as in Kolmogorov and Taylor–Couette flows (Armbruster *et al.* 1996; Coughlin & Marcus 1996). For all the sequences with different values of ζ in §§ 5–7, bursting is a characteristic feature of the transition from small-scale motion dominated by magnetic fields to broad irregular plumes where the Lorentz force is only locally important. This transition is associated with intermittent behaviour, related to trajectories that approach invariant subspaces corresponding to symmetrical solutions, as in figure 6(*c–f*). The dynamics displayed in figure 14(*a–d*) shows clear parallels with a recent experiment on convection in nematic liquid crystals (Peacock, Mullin & Binks 1999), where an ordered pattern of squares persists for a while before evolving into a weakly turbulent flow, which then reverts back into the original square pattern.

The computational results presented here as R is increased for fixed Q can be contrasted with those obtained previously by varying Q for fixed R. Weiss *et al.* (1996) set $\zeta = 1.2$, $R = 100\,000$ and $\lambda = 2$, and then decreased Q from a value strong enough to halt convection. They found transitions from irregular hexagons (with four plumes in the box) for $Q = 2\,000$ to aperiodic spatially modulated oscillations at $Q = 1\,500$ and then to broad chaotic plumes at $Q = 1\,000$ (identical with those described in § 5.2). With $Q = 500$ convection was more vigorous; instead of the broad magnetic network in figure 7 there were intense local concentrations linked by narrow sheets, and the pattern evolved rapidly with flux moving as a 'magnetic fluid'.

Given adequate computing power, it is preferable to obtain solutions in much larger boxes in order to minimize geometrical constraints. Computations with $\lambda \geqslant 8$ reveal patterns that are qualitatively different. We have already seen in § 5.4 that the flow can organize itself so that there are two phases (one magnetic and the other convective) separated by fronts. Within the almost field-free regions the broad and vigorous plumes are able to expand and split to form a cluster, in a manner reminiscent of exploding granules in the solar photosphere (Spruit, Nordlund & Title 1990; Rast 1995; Tao *et al.* 1998). Similar effects occur in two-dimensional configurations (Matthews & Cox 2000), where flux separation has been studied systematically for aspect ratios up to $\lambda = 16$ by Blanchflower *et al.* (1998). With $\zeta = 1.2$, $R = 100\,000$ and the same standard atmosphere, but with slightly more realistic boundary conditions, they found that flux separation appears over a wide range of field strengths. For $4\,000 \geqslant Q \geqslant 1750$ there are steady two-dimensional rolls, followed by spatially modulated oscillations for $1\,500 \geqslant Q \geqslant 750$. Flux separated solutions exist for $Q \leqslant 3\,000$ so there is a wide range with bistability. It is even possible to find isolated convective rolls from which magnetic flux has been expelled (convectons) for values of Q greater than that for the linear onset of convection (Blanchflower 1999). Results obtained from a systematic study of the three-dimensional problem with similar boundary conditions indicate that flux separation only occurs for an intermediate range of field strengths (Weiss, Proctor & Brownjohn 2000).

https://doi.org/10.1017/S0022112000001373 Published online by Cambridge University Press

Taken together, these investigations have extended our understanding of interactions between photospheric convection and magnetic fields in the Sun (Title 2000). To be sure, the numerical experiments involve idealized configurations, with relatively modest values of *Rm*, but the results can still be used to interpret the effects of different field strengths on convection. At one extreme, in the umbrae of sunspots and pores, where the imposed field is strong and almost vertical, normal convection is substantially inhibited. Within an umbra (with a field of 0.2–0.3 T) there is a population of short-lived bright features (umbral dots) whose number density increases with decreasing size (Sobotka, Brandt & Simon 1997*a*, *b*). The brightest structures resemble isolated plumes, embedded in a sea of weaker spatially modulated oscillations (Weiss *et al.* 1996, 2000; Blanchflower *et al.* 1998). Where there are no magnetic fields, convection cells are responsible for the solar granulation. High-resolution observations are now revealing the fine structure of intergranular magnetic fields (Title *et al.* 1992; Berger *et al.* 1995; Berger & Title 1996; Title 2000). There is a clear distinction between granules in regions that are magnetically quiet and those in plage regions, where the average field strength exceeds a critical value of about 0.015 T. Where there are plages, the granules are smaller and the fields are confined to a perforated network. These patches are surrounded by regions that are relatively field-free, where larger granules are able to swell and split. This is a clear example of flux separation (Tao *et al.* 1998), as shown in figure 10. Where the mean field is weak, magnetic flux moves rapidly through a network, as has been demonstrated in both compressible and Boussinesq configurations (Weiss *et al.* 1996, 2000; Cattaneo 1999). Thus the observed structures can indeed be related to computational results.

We thank Douglas Gough, Chris Jones and Edgar Knobloch for helpful suggestions, and we are grateful for perceptive and constructive comments from a referee. This research was supported by grants from PPARC, and A.M.R. held the Royal Astronomical Society's Norman Lockyer Fellowship while this work was done. The results for $\lambda = 4$ and $\lambda = 8$ in §§ 5 and 7 were obtained on the Hitachi SR-2201 at the University of Cambridge High Performance Computing Facility, and we are grateful to Louis Tao and Greg McMullan for their assistance with optimizing the code.

Appendix. Symmetry breaking on a square lattice

A.1. *Symmetry breaking: an elementary approach*

We first outline the approach developed by Proctor & Weiss (1993) to describe the symmetries and instabilities of two-dimensional rolls, with motion confined to the (x, z)-plane. In a stratified layer the eigenfunctions of the linear problem develop into two-dimensional roll solutions that are periodic in x, with m_x reflection symmetry about a fixed plane. These solutions have the Z_2 spatial symmetry group generated by this reflection (figure 2*c* shows the three-dimensional analogue of these rolls). An instability may preserve or break the reflection symmetry of the rolls. A *saddle-node bifurcation*, such as occurs at a turning point on a solution branch, does not involve any change of symmetry. Alternatively if m_x is broken (in a *pitchfork* bifurcation), two new asymmetric solutions are formed, one being a leftward travelling wave, and the other a rightward travelling wave, each of which is steady in a uniformly moving frame (cf. Landsberg & Knobloch 1991; Matthews *et al.* 1993).

Consider now a *Hopf* bifurcation from the rolls. The reflection symmetry may be preserved, leading to periodic vacillations. Breaking this symmetry leads to pulsating waves, which have the *spatiotemporal* symmetry of an m_x reflection combined with

https://doi.org/10.1017/S0022112000001373 Published online by Cambridge University Press

Broken symmetries	Symmetry group	Type of bifurcation	New solution
None	$\{E, m_x, t_x, t_e\}$	Saddle-node	Steady rolls
m_x, t_x	$\{E, t_e\}$	Pitchfork	Steady travelling waves
t_e, t_x	$\{E, m_x\}$	Hopf	Vacillations
m_x, t_e	$\{E, t_x\}$	Hopf	Pulsating waves

TABLE 9. Solutions that bifurcate from two-dimensional rolls.

	Broken symmetries	Symmetry group	Type of bifurcation	New solution (figure)
1	None	D_4	Saddle-node	Large squares (15a')
2	$m_x, m_y, m_d, m_{d'}$	$\{E, \rho, i, \rho^3\}$	Pitchfork	Pinwheel (15b')
3	ρ, ρ^3, m_x, m_y	$\{E, m_d, m_{d'}, i\}$	Pitchfork	Asymmetric squares (15c')
4	$\rho, \rho^3, m_d, m_{d'}$	$\{E, m_x, m_y, i\}$	Pitchfork	Asymmetric squares (15d')
5(i)	$\rho, \rho^3, m_d, m_{d'}, m_y, i$	$\{E, m_x\}$	'Double-zero'	Drifting squares
5(ii)	$\rho, \rho^3, m_d, m_{d'}, m_x, i$	$\{E, m_y\}$	'Double-zero'	Drifting squares (15e')
5(iii)	$\rho, \rho^3, m_d, m_x, m_y, i$	$\{E, m_{d'}\}$	'Double-zero'	Drifting squares
5(iv)	$\rho, \rho^3, m_{d'}, m_x, m_y, i$	$\{E, m_d\}$	'Double-zero'	Drifting squares (15f')

TABLE 10. Stationary bifurcations from large squares: note that the last four solutions generically bifurcate at the same point.

an advance of one-half of the period of the new time-dependent solution (Landsberg & Knobloch 1991; Matthews *et al.* 1993). Introducing a symmetry operation $t_e : (x, y, t) \to (x, y, t + \frac{1}{2}\Pi)$, which advances a half-period in time (Proctor & Weiss 1993), we can express the possibilities in terms of the symmetry group $\{E, m_x, t_e, t_x\}$, isomorphic to $Z_2 \otimes Z_2 = D_2$, where $t_x = t_e m_x$. The different solutions that arise are listed in table 9.

In the Boussinesq approximation there is an additional up–down symmetry that is lacking in a stratified layer, and the original eigenfunctions in the two-dimensional problem have D_2 spatial symmetry. Thus the fundamental steady solution has $D_2 \otimes Z_2 = D_{2h}$ spatiotemporal symmetry; this leads to a wider variety of possible bifurcations (cf. Proctor & Weiss 1993; Moore, Weiss & Wilkins 1991).

This approach can be extended to the three-dimensional problem with periodic boundary conditions. It gives a convincing description of the possibilities for stationary bifurcations from the large square pattern whose basic symmetry group is given by (3.1), though it is not immediately clear that this description is exhaustive; representation theory, described below, confirms that we have in fact covered all possibilities. Table 10 shows all the possible secondary patterns that can generically arise and most of these planforms are illustrated in figure 15. Note that the drifting solutions can also be reached after pitchfork bifurcations from solutions with D_2 symmetry; however, the Z_2-symmetric solution with symmetry $\{E, i\}$ can *only* appear after *two* successive bifurcations from D_4 symmetry. Similarly, solutions lacking all symmetry are only attainable after several bifurcations.

Hopf bifurcations are considerably more complicated. To understand all transitions we must introduce an additional time-shift symmetry $\hat{t}_e : (x, y, t) \to (x, y, t + \frac{1}{4}\Pi)$, where Π is the minimal period, which generates the group $\{E, \hat{t}_e, t_e, \hat{t}_e^3\} = Z_4$. So the full spatiotemporal symmetry group is $D_4 \otimes Z_4$ with 32 elements. (The theory of the next subsection explains why the quarter period is appropriate for all transitions.) Next we define the spatiotemporal symmetries $t_x = t_e m_x$, $t_\rho = t_e \rho$, etc. and $\hat{t}_x = \hat{t}_e m_x$,

https://doi.org/10.1017/S0022112000001373 Published online by Cambridge University Press

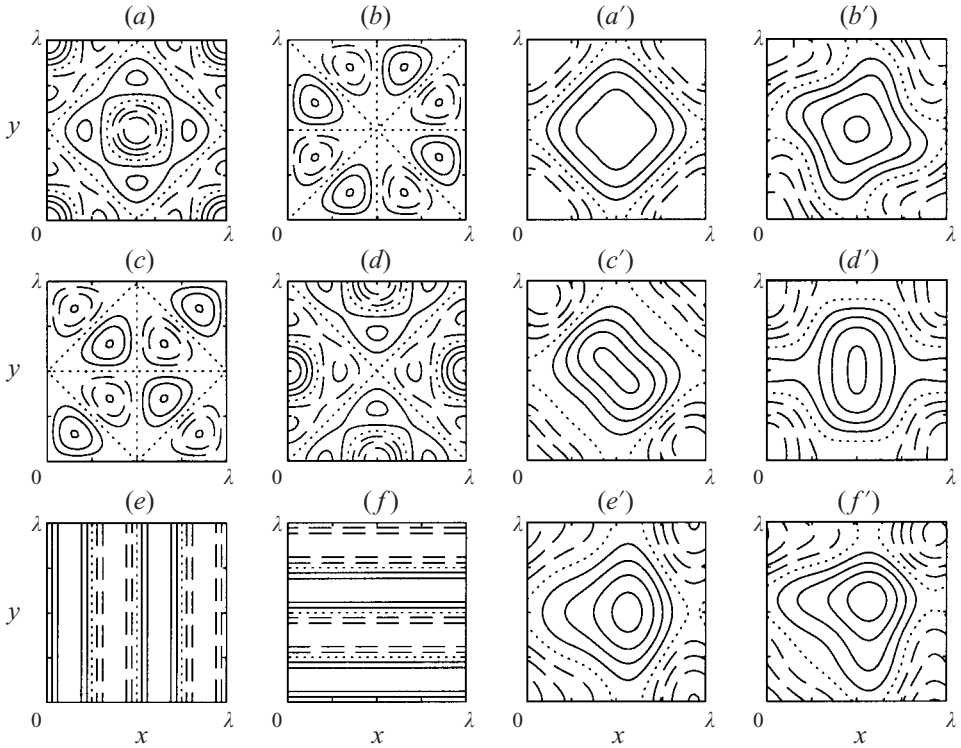


FIGURE 15. Stationary bifurcations from large squares with D_4 symmetry. The schematic plots in the left-hand panels show perturbations with different symmetries: (*a*) D_4; (*b*) Z_4 (pinwheel); (*c*) D_2 (diagonal); (*d*) D_2 (transverse); (*e*) Z_2 (travelling squares, *x*-direction); (*f*) Z_2 (travelling squares, *y*-direction). The right-hand panels show the perturbations from the left-hand panels added to large squares to give: (*a*′) D_4 (large squares); (*b*′) Z_4 (pinwheel); (*c*′) D_2 (diagonal asymmetric squares); (*d*′) D_2 (transversely asymmetric squares); (*e*′) Z_2 (transversely travelling squares); (*f*′) Z_2 (diagonally travelling squares). The patterns in (*a*′), (*b*′), (*c*′), (*d*′) and (*e*′) correspond to (*a*), (*b*), (*c*), (*d*) and (*e*), while (*f*′) corresponds to the sum of figures (*e*) and (*f*).

$\hat{t}_\rho = \hat{t}_e\rho$, etc. Table 11 lists the spatiotemporal oscillations that we may expect to find, together with the spatial symmetries that are broken. For instance, case 3 oscillates between the pattern in figure 15(*c*′) and its reflection half a period later. The pulsating or direction-reversing travelling wave solutions (Landsberg & Knobloch 1991; Matthews *et al.* 1993) have D_2 spatiotemporal symmetry so that e.g. in case 5(ii) the pattern in figure 15(*e*′) might move alternately to left and right, while case 5(i) involves a similar pattern moving up and down. Combining these two solutions with phase differences 0 or π yields cases 5(iii) and 5(iv) but if they are out of phase by $\frac{1}{2}\pi$ they combine to give the alternating pulsating waves (Matthews *et al.* 1996; Rucklidge 1997) of cases 5(v) and 5(vi). These are the counterparts of the alternating rolls that appear in a primary Hopf bifurcation with D_4 symmetry (Clune & Knobloch 1994). Note again that the *wobbler* solutions, introduced in §7.1, which have D_2 symmetries $\{E, i, t_x, t_y\}$, $\{E, i, t_d, t_{d'}\}$ or Z_4 symmetry $\{E, i, t_\rho, t_{\rho^3}\}$, can only appear after two successive bifurcations from the original D_4-symmetric state. This statement can be confirmed by the more formal treatment that follows, which provides an abstract but straightforward way of classifying possible transitions.

https://doi.org/10.1017/S0022112000001373 Published online by Cambridge University Press

	Broken symmetries	Symmetry group	New solution
1	None	$\{E, \rho, i, \rho^3, m_x, m_y, m_d, m_{d'}\}$	Vacillation
2	$m_x, m_y, m_d, m_{d'}$	$\{E, \rho, i, \rho^3, t_x, t_y, t_d, t_{d'}\}$	Oscillation
3	ρ, ρ^3, m_x, m_y	$\{E, m_d, m_{d'}, i, t_x, t_y, t_\rho, t_{\rho^3}\}$	Oscillation
4	$\rho, \rho^3, m_d, m_{d'}$	$\{E, m_x, m_y, i, t_d, t_{d'}, t_\rho, t_{\rho^3}\}$	Oscillation
5(i)	$\rho, \rho^3, m_d, m_{d'}, m_y, i$	$\{E, m_x, t_y, t_i\}$	Pulsating wave
5(ii)	$\rho, \rho^3, m_d, m_{d'}, m_x, i$	$\{E, m_y, t_x, t_i\}$	Pulsating wave
5(iii)	$\rho, \rho^3, m_d, m_x, m_y, i$	$\{E, m_{d'}, t_d, t_i\}$	Pulsating wave
5(iv)	$\rho, \rho^3, m_{d'}, m_x, m_y, i$	$\{E, m_d, t_{d'}, t_i\}$	Pulsating wave
5(v)	$\rho, \rho^3, m_d, m_{d'}, m_x, m_y, i$	$\{E, \hat{t}_\rho, t_i, \hat{t}^3_{\rho^3}\}$	Alternating pulsating wave
5(vi)	$\rho, \rho^3, m_d, m_{d'}, m_x, m_y, i$	$\{E, \hat{t}_{\rho^3}, t_i, \hat{t}^3_\rho\}$	Alternating pulsating wave

TABLE 11. Oscillatory bifurcations from large squares: if any of 5(i)–(vi) appears then all appear; other possible solutions may exist for certain parameter values (cf. Swift 1988).

A.2. *Linear theory: representations*

In this subsection, we discuss representations of groups, which describe the ways in which the marginally stable eigenfunctions at a bifurcation point are affected when symmetries are applied. As a parameter (say μ) is varied, a known steady solution might change from being stable to unstable. At the bifurcation point ($\mu = 0$), there are a number of marginally stable eigenfunctions $\xi_1, \ldots, \xi_n$, and the nonlinear dynamics near the bifurcation point can be described by evolution equations for the amplitudes $a_1(t), \ldots, a_n(t)$ of these eigenfunctions:

$$\dot{\boldsymbol{a}} = \boldsymbol{f}(\boldsymbol{a}; \mu) \tag{A 1}$$

where $\boldsymbol{a} = (a_1, \ldots, a_n)$. If the underlying solution is time-periodic the ODE (A 1) is replaced by a map, giving the amplitude of the perturbation after each period of the underlying solution.

The known solution is supposed to be invariant under all elements γ in the symmetry group Γ. This means that acting on a marginally stable eigenfunction with one of these symmetry elements will generate another marginally stable eigenfunction, so an operation γ takes $\boldsymbol{a}$ to $\boldsymbol{R}_\gamma \boldsymbol{a}$, where $\boldsymbol{R}_\gamma$ is an $n \times n$ matrix. The set of matrices $\boldsymbol{R}_\Gamma = \{\boldsymbol{R}_\gamma\}$ form a group called a *representation* of Γ, which depends on the symmetries of the eigenfunctions. Whenever $\gamma_1 \gamma_2 = \gamma_3$, the corresponding matrices obey $\boldsymbol{R}_{\gamma_1} \boldsymbol{R}_{\gamma_2} = \boldsymbol{R}_{\gamma_3}$, though the converse may not hold. Clearly, $\boldsymbol{R}_E$ is the unit matrix $\boldsymbol{I}$ in all representations. Note that the dimension n, which is the number of independent eigenfunctions, is not known in advance. Since the underlying solution is unchanged by $\gamma \in \Gamma$ we have the condition

$$\boldsymbol{f}(\boldsymbol{R}_\gamma \boldsymbol{a}) = \boldsymbol{R}_\gamma \boldsymbol{f}(\boldsymbol{a}), \tag{A 2}$$

for all $\gamma \in \Gamma$. When this holds, the system is said to be *equivariant* under Γ. Linearizing this equation we have the relation

$$\mathscr{L} \boldsymbol{R}_\gamma = \boldsymbol{R}_\gamma \mathscr{L}; \quad \mathscr{L} \equiv \frac{\partial \boldsymbol{f}}{\partial \boldsymbol{a}}(\boldsymbol{a} = 0, \mu = 0), \tag{A 3}$$

so that each $\boldsymbol{R}_\gamma$ commutes with $\mathscr{L}$.

We apply these ideas to secondary steady-state bifurcations from steady large squares, which are invariant under $\Gamma = D_4 = \{E, m_x, m_y, m_d, m_{d'}, \rho, i, \rho^3\}$, supposed to occur when a parameter $\mu = 0$. First consider one-dimensional representations,

https://doi.org/10.1017/S0022112000001373 Published online by Cambridge University Press

Figure	$\boldsymbol{R}_E$	$\boldsymbol{R}_{m_x}$	$\boldsymbol{R}_{m_d}$	$\boldsymbol{R}_{m_y}$	$\boldsymbol{R}_{m_{d'}}$	$\boldsymbol{R}_\rho$	$\boldsymbol{R}_{\rho^3}$	$\boldsymbol{R}_i$
1 15(a)	1	1	1	1	1	1	1	1
2 15(b)	1	−1	−1	−1	−1	1	1	1
3 15(c)	1	−1	1	−1	1	−1	−1	1
4 15(d)	1	1	−1	1	−1	−1	−1	1
5 15(e,f)	$\begin{bmatrix}1&0\\0&1\end{bmatrix}$	$\begin{bmatrix}-1&0\\0&1\end{bmatrix}$	$\begin{bmatrix}0&1\\1&0\end{bmatrix}$	$\begin{bmatrix}1&0\\0&-1\end{bmatrix}$	$\begin{bmatrix}0&-1\\-1&0\end{bmatrix}$	$\begin{bmatrix}0&-1\\1&0\end{bmatrix}$	$\begin{bmatrix}0&1\\-1&0\end{bmatrix}$	$\begin{bmatrix}-1&0\\0&-1\end{bmatrix}$

TABLE 12. The five irreducible representations of D_4, for stationary bifurcations from squares. The numbers in the first two columns correspond to those in tables 10 and 11.

in which the matrices $\boldsymbol{R}_\gamma$ are just numbers. There is always a trivial representation, with $\boldsymbol{R}_\gamma = 1$ for all γ. In this case, the eigenfunction is unchanged by any symmetry operation in D_4; an example of such a function is illustrated in figure 15(a).

There are three other one-dimensional representations. Taking m_x first, for example, we note that $m_x^2 = E$, so $\boldsymbol{R}_{m_x}^2 = 1$, or $\boldsymbol{R}_{m_x} = \pm 1$. In other words, either the eigenfunction is left unchanged by the reflection m_x, or it is sent to minus itself by the reflection. Similarly we have $\boldsymbol{R}_{m_d} = \pm 1$; so there are four possible combinations of the signs of $\boldsymbol{R}_{m_x}$ and $\boldsymbol{R}_{m_d}$. Once these are specified, all the others follow, since all group elements can be generated by m_x and m_d. For example, $\rho = m_x m_d$ so we have $\boldsymbol{R}_\rho = \boldsymbol{R}_{m_x}\boldsymbol{R}_{m_d}$. The other possibilities are given in table 12.

Note that the representations of D_4 in the table are consistent with the group multiplication of D_4 and that all new eigenfunctions obtained by acting on a marginal eigenfunction with an operation $\gamma \in \Gamma$ are multiples of the eigenfunction itself, so the symmetries do not in these cases force new linearly independent eigenfunctions. Thus there is only one eigenfunction associated with each of the instabilities we have been discussing. This is consistent with the assumption that the representation and the amplitude $\boldsymbol{a}$ are one-dimensional. We now suppose that there is more than one independent marginally stable eigenfunction $\xi_1, \xi_2, \ldots$, and that the marginally stable eigenfunction ξ_1 changes sign under m_x but is left invariant under m_y, as illustrated in figure 15(e). Reflecting this eigenfunction in the diagonal leads to a new, linearly independent, eigenfunction $\xi_2 = m_d\xi_1$ (figure 15f). This eigenfunction must also be marginally stable, since the underlying large squares are unchanged by this reflection. Further reflections and rotations lead to no new eigenfunctions, so the representations are 2×2 matrices and $\boldsymbol{a}$ is two-dimensional.

We have described five possible representations of D_4, which are summarized in table 12 (cf. Matthews 1999, who discusses these representations in the context of dynamo theory). There are group-theoretic results that guarantee that these are the only (absolutely, i.e. real) *irreducible* representations, characterized by the condition that the only matrices that commute with every matrix in the representation are multiples of the identity. This requirement guarantees that the marginal eigenvalues have the same multiplicity n as the dimension of the representation. Similar general results hold for every symmetry group. For a given finite group Γ, it is a straightforward matter to find the absolutely irreducible representations (see for example Riley, Hobson & Bence 1997).

A.3. *Nonlinear theory*

The dynamics near a bifurcation point $\mu = 0$ is governed by the dynamics of the amplitudes (A 1) of the marginally unstable modes at the bifurcation point (Centre

https://doi.org/10.1017/S0022112000001373 Published online by Cambridge University Press

Manifold Theorem; cf. Guckenheimer & Holmes 1983). We expand $\boldsymbol{f}(\boldsymbol{a};\mu)$ as a power series in $\boldsymbol{a}$ and μ, and use the equivariance condition (A 2) to eliminate terms in the expansion. The resulting normal form will depend on which representation arises at the bifurcation point. We illustrate with the steady-state D_4 problem above. Representations are referred to by their numbers in table 12.

1. No restrictions on the dynamics at the bifurcation point. Expanding f and changing coordinates yields the normal form for a saddle-node bifurcation:

$$\dot{a} = \mu + Ca^2 + \cdots, \tag{A 4}$$

where C is a constant. This corresponds to a pair of large square solutions (figure 15a'), with the same symmetries, colliding and annihilating.

2,3,4. Here we have some $\boldsymbol{R}_\gamma = -1$. These force f to be an odd function of (a), so, truncated to cubic order, we obtain the normal form for a pitchfork bifurcation:

$$\dot{a} = \mu a + Ca^3 + \cdots. \tag{A 5}$$

The new solutions are left unchanged by those symmetry elements γ that are represented by 1. This subgroup of Γ is called the isotropy subgroup (or the symmetry group) of the new branch of solutions. The symmetry groups of the various branches are given in table 9.

The two-dimensional representation (5 in table 12) results in the second-order normal form

$$\left.\begin{aligned} \dot{a}_1 &= \mu a_1 + Ca_1^3 + Da_1a_2^2 + \cdots, \\ \dot{a}_2 &= \mu a_2 + Ca_2^3 + Da_2a_1^2 + \cdots, \end{aligned}\right\} \tag{A 6}$$

where C and D are constants. Typically, $|C| \neq |D|$, and the equilibrium points of this set of ODEs are $(a,0)$ and $(0,a)$, with $a^2 = -\mu/C$, and (a,a) and $(a,-a)$, with $a^2 = -\mu/(C+D)$. The solution of type $(a,0)$ with isotropy subgroup $Z_2 = \{E, m_y\}$ is illustrated in figure 15(e'); figure 15(f') shows a solution of type (a,a) with isotropy subgroup $Z_2 = \{E, m_d\}$. The isotropy subgroups are made up of the symmetry elements that leave $(a,0)$ and (a,a) unchanged, that is, E and m_y in the first case, and E and m_d in the second.

These new solutions break enough symmetries that the pattern (in a periodic box) is now free to drift: the first drifts along the x-axis (since left is no longer equivalent to right), and the second along the diagonal (Rucklidge 1997). We can show that these travelling squares (either transverse or diagonal but not both) are stable only if both branches bifurcate supercritically.

The advantage of the group-theoretic approach is to enumerate all possibilities systematically, so that we know that the above five types are the only possible simple stationary bifurcations. We have thus confirmed (for instance) that not all subgroups of D_4 are possible symmetry groups of bifurcating solutions: in particular, $\{E, i\}$ is not an isotropy subgroup of any bifurcating solution. An alternative way of obtaining this information is to invoke the Equivariant Branching Lemma, for which we refer the interested reader to Golubitsky *et al.* (1988). This lemma greatly simplifies the calculations required to work out the bifurcating solutions and their isotropy subgroups. It is interesting to note that Bergeon, Henry & Knobloch (2000) find numerically four of the five representations as secondary instabilities of Bénard–Marangoni convection in a square container with no-slip sidewalls.

Similar considerations apply in the case of the Hopf bifurcation (with pure imaginary eigenvalues); here we invoke the Equivariant Hopf Theorem – see Golubitsky

https://doi.org/10.1017/S0022112000001373 Published online by Cambridge University Press

et al. (1988) for more details. We summarize the main results in the situation where a Hopf bifurcation breaks a reflection symmetry in the simplest possible way. Suppose that at such a Hopf bifurcation there are two marginally stable eigenfunctions ξ and $\bar{\xi}$ with eigenvalues $\mathrm{i}\omega$ and $-\mathrm{i}\omega$, and that the eigenfunction ξ has complex amplitude a. As above, symmetry operations γ act on a (and its complex conjugate $\bar{a}$) by multiplication by $\boldsymbol{R}_\gamma$, which in this discussion we take to be $+1$ or -1. In addition, advancing by time t takes a to $a\mathrm{e}^{\mathrm{i}\omega t}$. The combination of these two actions ($\boldsymbol{R}_\gamma$ and $\mathrm{e}^{\mathrm{i}\omega t}$) defines a representation of the group $\Gamma \otimes S^1$, where S^1 is the circle group corresponding to advances in time. As in the steady case, the symmetry group of the new, time-periodic solution created in the Hopf bifurcation is exactly the group of symmetry operations that are represented by $+1$. These will be purely spatial symmetries, with $\boldsymbol{R}_\gamma = +1$, as well as spatiotemporal symmetries, with $\boldsymbol{R}_\gamma = -1$ combined with a half-period (π/ω) time shift (since $\mathrm{e}^{\mathrm{i}\pi} = -1$). This justifies the introduction of the half-period time advance operation t_e by Proctor & Weiss (1993) when the relevant representation is made up entirely of $+1$ and -1.

To take a specific example, suppose that, in a Hopf bifurcation from a large square solution with $\Gamma = D_4$ spatial symmetry, the effect of the symmetry operations on the marginally stable eigenfunctions gives us representation 2 in table 12. Then the new time-periodic solution created in the Hopf bifurcation would have symmetry group $\{E, \rho, i, \rho^3, t_x, t_y, t_d, t_{d'}\}$, where the last four elements combine reflections with a half-period time advance. This solution would have the appearance of an oscillation between the pattern in figure 15(b') and a reflection of that pattern. Similar considerations yield solutions that oscillate between figure 15(c') and its 90° rotation, and between figure 15(d') and its 90° rotation. As before, the trivial representation occurs when no symmetry is broken, and the amplitude of large squares (figure 15a') would merely vacillate. Matters are considerably more complicated when the representation of Γ is complex or of greater dimension than unity; see Golubitsky *et al.* (1988). The specific case of a Hopf bifurcation from large squares was treated by Rucklidge (1997; see also Swift 1988), and the transverse pulsating squares, diagonal pulsating squares and alternating pulsating waves described in § A.1 are recovered. In this case, 90° rotations can be represented by $\pm\mathrm{i}$, and so to obtain unit spatiotemporal representations for the periodic solutions it is necessary (and sufficient) to combine rotations with quarter-period time shifts ($\mathrm{e}^{\pm\mathrm{i}\pi/2}$). In the general case, as for the stationary bifurcation, not all subgroups of $D_4 \otimes S^1$ occur as possible isotropy subgroups of bifurcating solutions; in particular, the wobblers, with symmetry group $\{E, i, t_x, t_y\}$, cannot arise in a direct bifurcation from large squares.

REFERENCES

Armbruster, D., Nicolaenko, B., Smaoui, N. & Chossat, P. 1996 Symmetries and dynamics for 2-D Navier–Stokes flow. *Physica* **95D**, 81–93.

Ashwin, P., Covas, E. & Tavakol, R. 1999 Transverse instability for non-normal parameters. *Nonlinearity* **12**, 563–577.

Ashwin, P. & Rucklidge, A. M. 1998 Cycling chaos: its creation, persistence and loss of stability in a model of nonlinear magnetoconvection. *Physica* **122D**, 134–154.

Auer, M., Busse, F. H. & Clever, R. M. 1995 Three-dimensional convection driven by centrifugal buoyancy. *J. Fluid Mech.* **301**, 371–382.

Bajaj, K. M. S., Liu, J., Naberhuis, B. & Ahlers, G. 1998 Square patterns in Rayleigh–Bénard convection with rotation about a vertical axis. *Phys. Rev. Lett.* **81**, 806–809.

Bergeon, A., Henry, D. & Knobloch, E. 2000 Three-dimensional Marangoni–Bénard flows in square containers. *Phys. Fluids* (in press).

https://doi.org/10.1017/S0022112000001373 Published online by Cambridge University Press

Berger, T. E., Schrijver, C. J., Shine, R. A., Tarbell, T. D., Title, A. M. & Scharmer, G. 1995 New observations of subarcsecond photospheric bright points. *Astrophys. J.* **454**, 531–544.

Berger, T. E. & Title, A. M. 1996 On the dynamics of small-scale solar magnetic elements. *Astrophys. J.* **463**, 365–371.

Blanchflower, S. M. 1999 Magnetohydrodynamic convectons. *Phys. Lett.* **261A**, 74–81.

Blanchflower, S. M., Rucklidge, A. M. & Weiss, N. O. 1998 Modelling photospheric magneto-convection. *Mon. Not. R. Astron. Soc.* **301**, 593–608.

Busse, F. H. 1972 The oscillatory instability of convection rolls in a low Prandtl number fluid. *J. Fluid Mech.* **52**, 97–112.

Busse, F. H. & Clever, R. M. 1998 Mechanisms of the onset of time-dependence in thermal convection In *Time-dependent Nonlinear Convection* (ed. P. A. Tyvand), pp. 1–49. Southampton: Computational Mechanics Publications.

Busse, F. H. & Müller, S. C. (Eds.) 1998 *Evolution of Spontaneous Structures in Dissipative Continuous Systems.* Springer.

Cattaneo, F. 1999 On the origin of magnetic fields in the quiet photosphere. *Astrophys. J.* **515**, L39–L42.

Cattaneo, F., Brummell, N. H., Toomre, J., Malagoli, A. & Hurlburt, N. E. 1991 Turbulent compressible convection. *Astrophys. J.* **370**, 282–294.

Chossat, P. & Lauterbach, R. 2000 *Methods in Equivariant Bifurcations and Dynamical Systems.* World Scientific.

Clune, T. & Knobloch, E. 1994 Pattern selection in three-dimensional magnetoconvection. *Physica* **74D**, 151–176.

Coughlin, K. & Marcus, P. S. 1996 Turbulent bursts in Couette–Taylor flow. *Phys. Rev. Lett.* **77**, 2214–2217.

Crawford, J. D. & Knobloch, E. 1991 Symmetry and symmetry-breaking bifurcations in fluid dynamics. *Ann. Rev. Fluid Mech.* **23**, 341–387.

Croquette, V. & Williams, H. 1989 Nonlinear competition between waves on convective rolls. *Phys. Rev.* A **39**, 2765–2768.

Dionne, B., Silber, M. & Skeldon, A. C. 1997 Stability results for steady, spatially periodic planforms. *Nonlinearity* **10**, 321–353.

Eckert, K., Bestehorn, M. & Thess, A. 1998 Square cells in surface-tension-driven Bénard convection: experiment and theory. *J. Fluid Mech.* **356**, 155–197.

Edwards, W. S. & Fauve, S. 1994 Patterns and quasi-patterns in the Faraday experiment. *J. Fluid Mech.* **278**, 123–148.

Golubitsky, M., Stewart, I. & Schaeffer, D. G. 1988 *Singularities and Groups in Bifurcation Theory. Volume II.* Springer.

Gough, D. O., Moore, D. R., Spiegel, E. A. & Weiss, N. O. 1976 Convective instability in a compressible atmosphere. II. *Astrophys. J.* **206**, 536–542.

Guckenheimer, J. & Holmes, P. 1983 *Nonlinear Oscillations, Dynamical Systems and Bifurcations of Vector Fields.* Springer.

Hirschberg, P. & Knobloch, E. 1993 Zigzag and varicose instabilities of a localized stripe *Chaos* **3**, 713–721.

Hoyle, R. B. 1998 Universal instabilities of rolls, squares and hexagons. In *Time-dependent Nonlinear Convection* (ed. P. A. Tyvand), pp. 51–82. Southampton: Computational Mechanics Publications.

Hurlburt, N. E., Proctor, M. R. E., Weiss, N. O. & Brownjohn, D. P. 1989 Nonlinear compressible magnetoconvection. Part 1. Travelling waves and oscillations. *J. Fluid Mech.* **207**, 587–628.

Hurlburt, N. E. & Toomre, J. 1988 Magnetic fields interacting with nonlinear compressible convection. *Astrophys. J.* **327**, 920–932.

Knobloch, E. & Moehlis, J. 1999 Bursting mechanisms for hydrodynamical systems. In *Pattern Formation in Continuous and Coupled Systems.* (ed. M. Golubitsky, D. Luss & S. H. Strogatz), pp. 157–174. Springer.

Kudrolli, A., Pier, B. & Gollub, J. P. 1998 Superlattice patterns in surface waves. *Physica* **123D**, 99–111.

Landsberg, A. S. & Knobloch, E. 1991 Direction-reversing traveling waves. *Phys. Lett.* **159A**, 17–20.

Matthews, P. C. 1998 Hexagonal patterns in finite domains. *Physica* **116D**, 81–94.

https://doi.org/10.1017/S0022112000001373 Published online by Cambridge University Press

Matthews, P. C. 1999 Dynamo action in simple convective flows. *Proc. R. Soc. Lond.* A **455**, 1829–1840.

Matthews, P. C. & Cox, S. M. 2000 Pattern formation with a conservation law. *Nonlinearity* **13**, 1293–1320.

Matthews, P. C., Proctor, M. R. E., Rucklidge, A. M. & Weiss, N. O. 1993 Pulsating waves in nonlinear magnetoconvection. *Phys. Lett.* **183A**, 69–75.

Matthews, P. C., Proctor, M. R. E. & Weiss, N. O. 1995 Compressible magnetoconvection in three dimensions: planforms and nonlinear behaviour. *J. Fluid Mech.* **305**, 281–305 (referred to herein as Paper I).

Matthews, P. C., Rucklidge, A. M., Weiss, N. O. & Proctor, M. R. E. 1996 The three-dimensional development of the shearing instability of convection. *Phys. Fluids* **8**, 1350–1352.

McKenzie, D. 1988 The symmetry of convective transitions in space and time. *J. Fluid Mech.* **191**, 287–339.

Meneguzzi, M., Sulem, C., Sulem, P. L. & Thual, O. 1987 Three-dimensional numerical simulation of convection in low-Prandtl-number fluids. *J. Fluid Mech.* **182**, 169–191.

Moehlis, J. & Knobloch, E. 1998 Forced symmetry breaking as a mechanism for bursting. *Phys. Rev. Lett.* **80**, 5329–5332.

Moore, D. R. & Weiss, N. O. 2000 Resonant interactions in thermosolutal convection. *Proc. R. Soc. Lond.* A **456**, 39–62.

Moore, D. R., Weiss, N. O. & Wilkins, J. M. 1991 Asymmetric oscillations in thermosolutal convection. *J. Fluid Mech.* **233**, 561–585.

Moses, E. & Steinberg, V. 1991 Stationary convection in a binary mixture. *Phys. Rev.* A **43**, 707–722.

Oliver, D. S. & Booker, J. R. 1983 Planform of convection with strongly temperature-dependent viscosity. *Geophys. Astrophys. Fluid Dyn.* **27**, 73–85.

Ondarçuhu, T., Mindlin, G. B., Mancini, H. L. & Pérez-García, C. 1993 Dynamical patterns in Bénard–Marangoni convection in a square container. *Phys. Rev. Lett.* **70**, 3892–3895.

Peacock, T., Mullin, T. & Binks, D. J. 1999 Bifurcation phenomena in flows of a nematic liquid crystal. *Intl J. Bifurcation Chaos* **9**, 427–441.

Platt, N., Spiegel, E. A. & Tresser, C. 1993 On-off intermittency: a mechanism for bursting. *Phys. Rev. Lett.* **70**, 279–282.

Proctor, M. R. E. & Matthews, P. C. 1996 $\sqrt{2}$:1 Resonance in non-Boussinesq convection. *Physica* **97D**, 229–241.

Proctor, M. R. E. & Weiss, N. O. 1982 Magnetoconvection. *Rep. Prog. Phys.* **45**, 1317–1379.

Proctor, M. R. E. & Weiss, N. O. 1993 Symmetries of time-dependent magnetoconvection. *Geophys. Astrophys. Fluid Dyn.* **70**, 137–160.

Proctor, M. R. E., Weiss, N. O., Brownjohn, D. P. & Hurlburt, N. E. 1994 Nonlinear compressible magnetoconvection. Part 2. Streaming instabilities in two dimensions. *J. Fluid Mech.* **280**, 227–253.

Proctor, M. R. E., Weiss, N. O. & Matthews, P. C. 1996 Magnetoconvection in deep fluid layers. In *Advances in Multi-Fluid Flows* (ed. Y. Y. Renardy, A. V. Coward, D. T. Papageorgiou & S.-M. Sun), pp. 399–414. SIAM.

Rast, M. P. 1995 On the nature of 'exploding' granules and granule fragmentation. *Astrophys. J.* **443**, 863–868.

Riley, K. F., Hobson, M. P. & Bence, S. J. 1997 *Mathematical Methods for Physics and Engineering: a Comprehensive Guide*. Cambridge University Press .

Rucklidge, A. M. 1997 Symmetry-breaking instabilities of convection in squares. *Proc. R. Soc. Lond.* A **453**, 107–118.

Rucklidge, A. M. & Matthews, P. C. 1996 Analysis of the shearing instability in nonlinear convection and magnetoconvection. *Nonlinearity* **9**, 311–351.

Rucklidge, A. M. & Silber, M. 1998 Bifurcations of periodic orbits with spatio-temporal symmetries. *Nonlinearity* **11**, 1435–1455.

Silber, M. & Knobloch, E. 1991 Hopf bifurcation on square lattices. *Nonlinearity* **4**, 1063–1106.

Sobotka, M., Brandt, P. N. & Simon, G. W. 1997*a* Fine structure in sunspots. I. Sizes and lifetimes of umbral dots. *Astron. Astrophys.* **328**, 682–688.

https://doi.org/10.1017/S0022112000001373 Published online by Cambridge University Press

Sobotka, M., Brandt, P. N. & Simon, G. W. 1997*b* Fine structure in sunspots. II. Intensity variations and proper motions of umbral dots. *Astron. Astrophys.* **328**, 689–694.

Spruit, H. C., Nordlund, Å. & Title, A. M. 1990 Solar convection. *Ann. Rev. Astron. Astrophys.* **28** 263–301.

Stein, R. F. & Nordlund, Å. 1998 Simulations of solar convection. I. General properties. *Astrophys. J.* **499**, 914–933.

Sullivan, T. S. & Ahlers, G. 1988 Nonperiodic time dependence at the onset of convection in a binary fluid mixture. *Phys. Rev.* A **38**, 3143–3146.

Swift, J. W. 1988 Hopf bifurcation with the symmetry of a square. *Nonlinearity* **1**, 333–377.

Tao, L., Weiss, N. O., Brownjohn, D. P. & Proctor, M. R. E. 1998 Flux separation in stellar magnetoconvection. *Astrophys. J.* **496**, L39–L42.

Title, A. M. 2000 Magnetic fields below, on and above the solar surface. *Phil. Trans. R. Soc. Lond.* A **358**, 657–668.

Title, A. M., Topka, K. P., Tarbell, T. D., Schmidt, W., Balke, C. & Scharmer, G. 1992 On the differences between plage and quiet Sun in the solar photosphere. *Astrophys. J.* **393**, 782–794.

Tse, D. P., Rucklidge, A. M., Hoyle, R. B. & Silber, M. 2000 Secondary instabilities of standing hexagons in a Faraday wave experiment. *Physica* D (in press).

Weiss, N. O., Brownjohn, D. P., Hurlburt, N. E. & Proctor, M. R. E. 1990 Oscillatory convection in sunspot umbrae. *Mon. Not. R. Astron. Soc.* **245**, 434–452.

Weiss, N. O., Brownjohn, D. P., Matthews, P. C. & Proctor, M. R. E. 1996 Photospheric convection in strong magnetic fields. *Mon. Not. R. Astron. Soc.* **283**, 1153–1164.

Weiss, N. O., Proctor, M. R. E. & Brownjohn, D. P. 2000 Magnetic flux separation in photospheric convection. To be submitted to *Mon. Not. R. Astron. Soc.*

https://doi.org/10.1017/S0022112000001373 Published online by Cambridge University Press